JCB Journal of Cell Biology

REPORT

Hyperstabilization of T cell microvilli contacts by chimeric antigen receptors

Casey Beppler[1], John Eichorst[2], Kyle Marchuk[2], En Cai[1], Carlos A. Castellanos[3], Venkataraman Sriram[4], Kole T. Roybal[5,6,7,8*], and Matthew F. Krummel[1*]

T cells typically recognize their ligands using a defined cell biology—the scanning of their membrane microvilli (MV) to palpate their environment—while that same membrane scaffolds T cell receptors (TCRs) that can signal upon ligand binding. Chimeric antigen receptors (CARs) present both a therapeutic promise and a tractable means to study the interplay between receptor affinity, MV dynamics and T cell function. CARs are often built using single-chain variable fragments (scFvs) with far greater affinity than that of natural TCRs. We used high-resolution lattice lightsheet (LLS) and total internal reflection fluorescence (TIRF) imaging to visualize MV scanning in the context of variations in CAR design. This demonstrated that conventional CARs hyper-stabilized microvillar contacts relative to TCRs. Reducing receptor affinity, antigen density, and/or multiplicity of receptor binding sites normalized microvillar dynamics and synapse resolution, and effector functions improved with reduced affinity and/or antigen density, highlighting the importance of understanding the underlying cell biology when designing receptors for optimal antigen engagement.

Introduction

Dynamic microvilli (MV) on T cells are critical for the cell's antigen search process (Orbach and Su, 2020; Pettmann et al., 2018). During early immunological synapse (IS) formation, MV enable close contact with antigen-presenting surfaces and are stabilized upon cognate antigen binding (Cai et al., 2017). Furthermore, MV promote kinetic segregation of phosphatases away from signaling domains (Razvag et al., 2018), and the formation and confinement of MV are sufficient for T cell activation in the absence of TCR agonists (Aramesh et al., 2021). TCR signaling at the prototypical IS, studied in 2D on supported lipid bilayers (SLBs), involves the accumulation of signaling components colocalizing with TCR microclusters (MCs). After a few minutes, MCs internalize (Friedl et al., 2005; Friedman et al., 2010) and/or migrate toward the center of the IS, where active kinases are rare (Campi et al., 2005; Grakoui et al., 1999; Monks et al., 1998; Varma et al., 2006). More recent work has revealed that TCR MC form on the tips of dynamically probing MV, facilitating their stabilization, and it is upon these MV protrusions that MCs move laterally within the early IS (Cai et al., 2017).

Chimeric antigen receptor-bearing T cells (CAR T cells) present both a therapeutic promise, given their success in treating B cell malignancies (Kalos et al., 2011; Brentjens et al., 2013; Maude et al., 2014), and a tractable system for understanding how affinity and avidity affect topographical synapse antigen scanning, given that they are easily engineered molecules. Typical CAR antigen binding domains (tumor antigen-binding scFvs) bind with nano- and even picomolar affinities, whereas TCRs bind agonist peptide-major histocompatibility complex (pMHC) with micromolar affinity (Stone et al., 2009), although co-receptors improve their functional binding strength (Garcia et al., 1996). The effect of such variation in binding on the dynamics of topographical antigen scanning is unknown. This is an especially interesting question given that CARs generate inefficient intracellular signaling relative to TCRs (Harris et al., 2018; Gudipati et al., 2020; Salter et al., 2021). It, therefore, seems plausible that improving the already ultra-high affinity binding might be beneficial. On the other hand, the currently favored model for T cell activation, supported by most experimental data, implies a penalty for TCR binding events that last too long (Lever et al., 2014). We thus sought to understand how CARs interact with the natural cell biology, relative to TCRs, and how varying the binding

[1]Department of Pathology and ImmunoX, University of California, San Francisco, San Francisco, CA, USA; [2]Biological Imaging Development CoLab, University of California, San Francisco, San Francisco, CA, USA; [3]Department of Microbiology and Immunology, Sandler Asthma Basic Research Center, University of California, San Francisco, San Francisco, CA, USA; [4]Foundery Innovations, San Francisco, CA, USA; [5]Department of Microbiology and Immunology, University of California, San Francisco, San Francisco, CA, USA; [6]Parker Institute for Cancer Immunotherapy, San Francisco, CA, USA; [7]Chan Zuckerberg Biohub, San Francisco, CA, USA; [8]Helen Diller Comprehensive Cancer Center, San Francisco, CA, USA.

*K.T. Roybal and M.F. Krummel contributed equally to this paper. Correspondence to Matthew F. Krummel: matthew.krummel@ucsf.edu.

dynamics of an antigen receptor affects topographical antigen scanning.

Here, we combined high-resolution LLS and synaptic contact mapping (SCM) TIRF imaging—first, to establish the distribution of CAR relative to TCR on the T cell surface, and second, to establish the effects of receptor affinity and avidity on topographical scanning dynamics. To study effects of receptor affinity and avidity in isolation, point mutations were incorporated into the extracellular domains while all other aspects of CAR design were held constant—hinge and transmembrane domain (CD8), co-stimulatory domain (4-1BB), and CD3ζ signaling domain. In doing so, we found that CARs distributed similarly to TCRs. However, CARs based on conventional picomolar high-affinity dimers yielded hyperstabilization of the underlying MV relative to that of the natural TCR, which could be improved by reducing receptor affinity or avidity. Hyperstabilization was correlated with aberrant synapse resolution, and for dimers, decreased effector function and increased propensity for exhaustion.

Results and discussion

TCR and CAR distribution relative to microvilli on isolated T cells

TCRs have been reported to form patches (Lillemeier et al., 2006; Hu et al., 2016; Cai et al., 2022) and localize to MV to varying degrees (Jung et al., 2016; Cai et al., 2017, 2022). We expressed anti-HER2 CARs in primary human CD8⁺ T cells by lentiviral transduction and first sought to compare how they distribute on the cell surface, compared to natural TCR. To do this, we fixed CAR T cells, stained with antibodies to TCR and CAR, and imaged them by LLS. Visually, this revealed that CARs were distributed across the cell surface with patches of increased fluorescence intensity, similar to that of TCR, although not necessarily overlapping in position (Fig. 1, A–C, Fig. S1, A and B; and Video 1). Although examined here on fixed cells, similar patches have been described for TCRs by LLS using live imaging (Cai et al., 2022), where tracking analysis revealed that these patches are long-lived. While random fluctuations can result in an appearance of clustering, and thus may contribute to a subset of the features identified here (Rossboth et al., 2018), it is unlikely that a random distribution would produce patches whose diffusion can be tracked through time. Here, typical patches of TCR are estimated to include ∼5–20 TCRs per patch (Fig. S1, C and D), and all data is diffraction limited, as opposed to previous studies that addressed the existence of TCR oligomers at molecular resolution (Schamel et al., 2005; Kumar et al., 2011; Brameshuber et al., 2018). Taken together, it is likely that TCRs are concentrated within the patch although not directly associated. Here, we focus on the comparison between patches of CAR and TCR.

Zooming in to a region of the cell membrane, MV were noted as variably high for CAR alone, TCR alone, or both (Fig. 1 B and Fig. S1 E). About half of MV tips observed were high for TCR, and most but not all (83%) MV tips were CAR high (Fig. 1 C and Fig. S1 F), likely resulting from high CAR expression induced by lentiviral expression. Random distribution of CAR and TCR based off these proportions would predict ∼40% co-occupied tips. By our count, 32% of tips are co-occupied, consistent with co-occupancy being a random event. Thus, while TCR patches observed by LLS have been shown to overlap with the patches formed by other molecules like co-receptor CD8 (Cai et al., 2022), we do not see such a pattern for TCR with CAR.

Of note, TCR high, CAR high, and TCR/CAR high patch-like regions could be seen in both tips and areas of cell cortex, here referring to the regions on the body of the cell between MV (Fig. 1, D and E). To quantify this patchiness, the fluorescence intensity at the membrane was mapped to radial intensity profiles and a moving average of 10 pixels (∼3°) was applied (Fig. 1 F and Fig. S1 G). Using this method, patches of increased local fluorescence were identified for TCRs, as expected (Hu et al., 2016), but less so for the abundant CD45 molecule. CARs were found to form patches at frequencies similar to TCRs (Fig. 1 G) despite not obligately co-localizing.

To assess TCR and CAR patches relative to surface curvature in 3D, membrane curvature was mapped based on CD45 and regions of high convexity were thresholded to show MV (Fig. 2, A and B; and Fig. S1 H). CAR and TCR patches were assigned by identifying individual domains of locally high intensity along the cell boundary using Pearson correlation calculations for variable sized kernels followed by segmentation and watershed (Cai et al., 2022; Fig. 2, C and D; and Fig. S1 H). Thus, the 3D patch analysis was not dependent on global signal intensity thresholding, but instead identified patches based on local changes in fluorescence intensity. Surface areas of individual patches were then mapped by color (Fig. 2, E and F). We observed similar patch surface areas for TCR and CAR, with median sizes of 0.34 μm^2 (TCR) and 0.38 μm^2 (CAR; Fig. 2 G). Surface curvature values were mean-centered and both TCR and CAR patch localization were similarly mean-centered, indicating no preference for patches to reside in regions of high or low surface curvature (Fig. 2 H). 2D projections of the 3D surface curvature and antigen receptor intensity revealed regions of membrane tips and valleys both with and without antigen receptor (Fig. 2 I). Total number of identified patches was similar for CAR and TCR in a given cell, and the majority of patches for each receptor had <50% overlap with patches of the other (Fig. S1, I and J).

CAR enrichment at synaptic microvillar close contacts

To determine the location of CARs following interaction with a target cell, live anti-HER2 CAR T cells were added to coverslips with HER2+ SKBR3 cells and imaged by LLS at intervals of 4.7–6.75 s (Fig. 3, A–C, Fig. S2, A and B; and Video 2). This live cell imaging revealed accumulation of CAR patches at projections into the IS.

To further study the localization of CARs to these MV close contacts, mEmerald-tagged CAR T cells were analyzed on HER2-loaded SLBs using SCM TIRF microscopy. This method allows for facile visualization of both surface-localized receptors by TIRF, and the location of MV close contacts, seen by holes in fluorescent quantum dot (QD605) signal (Fig. 3 D). As previously demonstrated for TCR (Cai et al., 2017), CAR MCs formed and localized to areas of MV close contacts, as seen by segregation between the two signals (Fig. 3, E and F; and Fig. S2, D and G). As

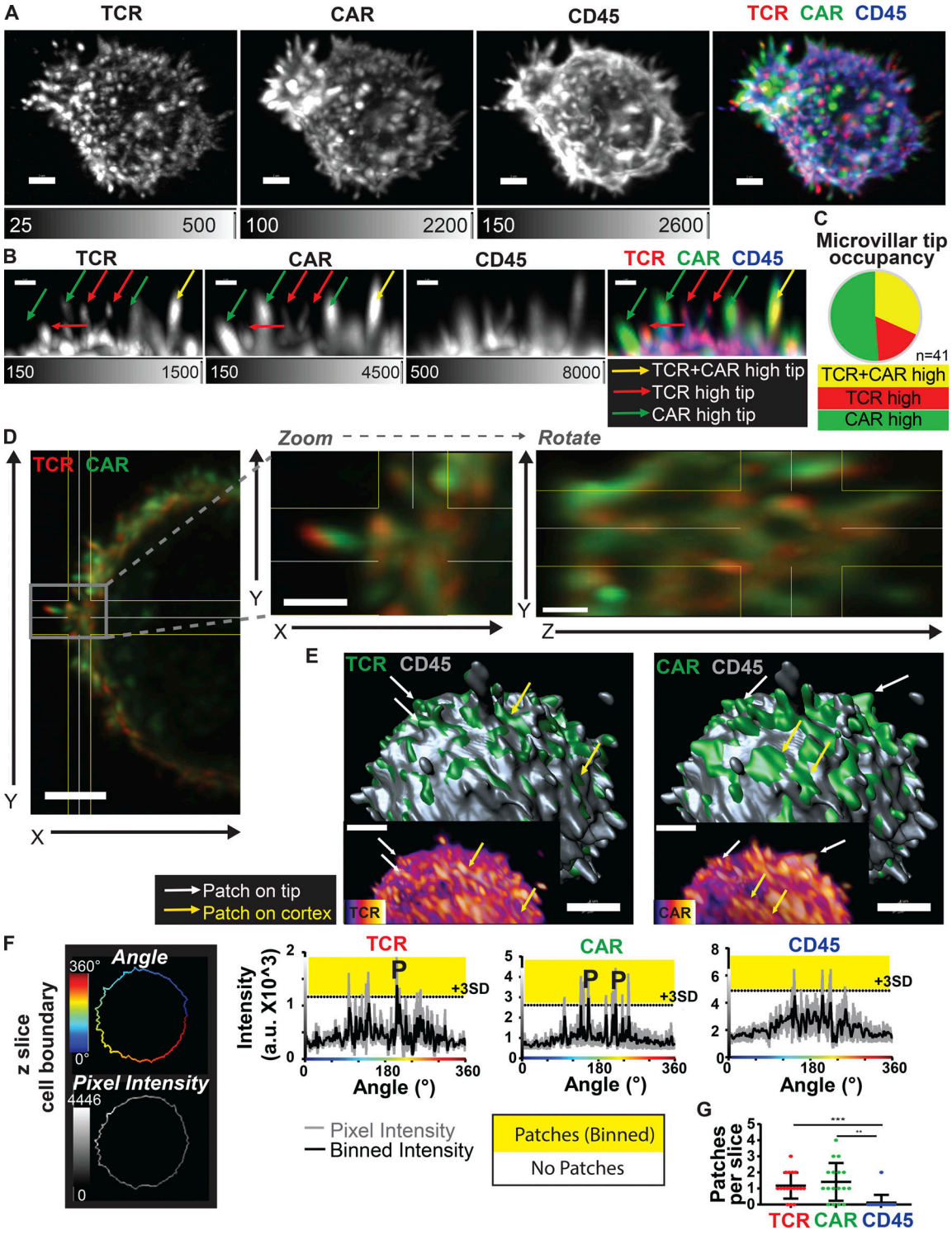

Figure 1. **CARs distribute similarly to TCRs on both microvilli and cell cortex, but do not obligately co-localize. (A)** Fixed anti-HER2 CAR T cell showing maximum intensity projection of TCR, CAR, CD45 and overlay imaged by lattice light-sheet. Scale bar = 2 µm. Human CD8⁺ T cell expressing anti-HER2 CAR (mut4D5) was labeled with antibodies to MYC (CAR)-Alexa488, TCR (OKT3)-APC, and CD45-Alexa594. **(B)** Region of cell membrane, as described in A, where MV tips are marked as being high for TCR (red arrow), CAR (green arrow), or both (yellow arrow). Scale bar = 1 µm. **(C)** 41 tips across 5 regions and 3 cells were scored as in B. **(D)** Left panel shows zoomed out membrane region in extended view for multiple *z* slices of a cell labeled as described in A (scale bar = 3 µm). Middle panel shows zoom in on outlined region (scale bar = 1 µm). Right panel shows the same zoom region with the perspective rotated to show the YZ plane (scale bar = 1 µm). **(E)** Large panels show CD45 surface (gray) overlaid with TCR (left) and CAR (right) surfaces marking areas of high intensity (green). Arrows mark examples of patches on MV tips (white) or cell cortex (yellow). Inset panels show a region of the same cell with the raw TCR and CAR intensity in Fire colorscale. Scale bar = 4 µm. **(F)** Left: Schematic showing the cell boundary as mapped to radial intensity profile by angle (x-axis) and pixel intensity (y-axis). Right: Pixel intensity (gray line) and binned intensity (black line), defined by taking a moving average of 10 pixels (~3°), showing one *z*-slice for TCR, CAR, and

CD45. Dashed line with yellow above indicates 3 standard deviations (+3SD) above mean pixel intensity. P indicates binned intensity peaks above +3SD threshold (patches). **(G)** Number of patches/z-slice for each receptor was defined by the number of excursions of binned intensity above the +3SD threshold. Tukey's multiple comparisons test was performed on data compiled from multiple slices of 3 cells (n = 17 slices per group). Error bar represents SD.

with TCR, not all MV close contacts at the IS were occupied by CAR MC (Fig. S2 C). To determine whether this localization was dependent simply on the formation of a stabilized close-contact or depended specifically on binding of CAR to its ligand, anti-HER2 CARs were expressed in OT-I mouse T cells and allowed to interact with SLBs loaded with only the TCR ligand, pMHC:SL8 (SIINFEKL). In these HER2-negative synapses, MV contacts formed but CARs did not accumulate as MC nor localize within those contacts (Fig. 3, G and H; and Fig. S2, E, H, and K). While differences in acquisition time relative to LLS imaging could contribute to molecular blurring within the imaging plane, the distinct lack of CAR patches at the TCR-stimulated IS may result from CAR patch exclusion due to molecular crowding by TCR and other engaged signaling receptors. Importantly, when the same mouse CAR T cells interacted with CAR antigen, we observed the same pattern as seen in human CAR-stimulated synapses (Fig. S2, F, I, and J). Thus, the recruitment of CAR MC to MV close contacts relied upon binding of CAR antigen, and TCR engagement was not sufficient to coordinate the CAR's reorganization at the interface.

Effects of affinity and avidity of receptor binding on synaptic microvillar dynamics

We next sought to understand how MV close contacts, hallmarks of TCR-induced activation (Cai et al., 2017; Farrell et al., 2020), were modulated by the affinity of the antigen receptor. To do this, we compared the wild-type high-affinity scFv (4D5) with a mutated scFv of ∼70-fold reduced affinity (mut4D5, Fig. 4 A and Table S1). We then analyzed MV close contacts by SCM at high temporal resolution in the presence of a range of ligand densities to measure MV persistence times (Fig. 4, B–D). Ligand densities were standardized against two breast cancer cell lines that differed significantly in their HER2 levels, and addition of 62.5 ng per 0.7 cm^2 well yielded expression levels comparable to a cell line representing healthy breast tissue, MCF7 (Liu et al., 2015; Comsa et al., 2015; Fig. S3, A and B). In the examples in Fig. 4 C and Video 3, individual MV close contacts mediated by low-HER2 SLBs remained stable in the case of a high-affinity (HA) CAR contact, while the low-affinity (LA) CAR close contact dispersed within seconds. Quantifying the lifetime of individual MV close contacts revealed that the persistence time of CAR-occupied close contacts increases with ligand density for LA CARs, but that HA CAR resulted in very stable contacts at all tested ligand densities (Fig. 4 D). All conditions tested induced stabilization of MV above background non-receptor-occupied contacts, which had uniformly short persistence times. Notably, at high HER2 density, the persistence of LA CAR close contacts reached ∼17 s on average, a value that was achieved by HA CAR even at 100× lower antigen densities—lower even than the low-HER2 MCF7 standard. Importantly, both low (62.5 ng/well) and high (625 ng/well) antigen densities led to calcium flux for both receptors (Fig. S3, C and D; and Video 4). At high density of antigen, Fura-2 ratiometric imaging demonstrated a decrease in the magnitude of the maximal ratio achieved, specifically for HA CAR (Fig. S3 D), suggesting altered signaling dynamics in the HA setting.

To directly compare CAR- and TCR-mediated persistence times, we expressed the LA CAR in OT-I mouse T cells and compared interactions with SL8:pMHC- and HER2-loaded SLBs. On SLBs with SL8:pMHC, normalized to levels displayed on APCs (Beemiller et al., 2012a), we measured TCR-mediated persistence to be an average of 12.3 s. LA CAR with low-HER2 SLBs yielded similar persistence times whereas persistence times on high HER2 were again found to be significantly greater (Fig. 4 E). We hypothesized that we could further engineer the LA CAR to yield TCR-like persistence times in high antigen-density conditions by minimizing CAR avidity contributions. Thus, we created a monomeric CAR by incorporating two cysteine to serine point mutations in the CD8α hinge to prevent formation of the disulfide bridge (Hennecke and Cosson, 1993; Fig. S3 E). Comparing monomers to dimers on high HER2-loaded SLBs (625 ng/well) revealed that only LA monomers produced MV persistence similar to that of the TCR (Fig. 4 F). Average CAR fluorescence intensity of close contacts was not significantly different between monomers and dimers and did not appear to correlate with persistence times under the conditions tested (Fig. S3, F and G).

Hyperstable microvillar dynamics are associated with altered synapse resolution, decreased effector function, and increased propensity for exhaustion

TCR-mediated IS formed on antigen-loaded SLBs result in TCR MC formation and radial motion toward the center (Campi et al., 2005; Yokosuka et al., 2005; Varma et al., 2006). Although alternative IS architectures characterized by the formation of CAR MC without centripetal movement have been revealed for CAR-mediated synapses (Davenport et al., 2018), we sought to relate binding dynamics resulting in hyperstabilization of MV to IS dynamics and centralization. Measurement of the distance across T cell MC following TIRF imaging of synapses—a means of assessing centralization—revealed that dimeric CAR MC only formed a central dense cluster under conditions of LA and low antigen density, whereas the monomers reliably formed this structure (Fig. 5, A and B).

To determine whether this phenotype was the result of a lack of mobility of MC, as opposed to direct accumulation of CARs in the center vs. periphery, we tracked the MC over time (Fig. S4 A; and Videos 5, 6, 7, 8, 9, and 10). On high-HER2 SLBs, the LA CAR monomer yielded mobile MC, whereas both CAR dimers showed impaired mobility as demonstrated by flower plots of MC displacement, and analysis of displacement and speed (Fig. 5, C and D; and Fig. S4, B and C). The mobility of LA but not HA CAR dimer MC was restored on low HER2-loaded SLBs. Analysis of the direction of MC movement revealed no significant

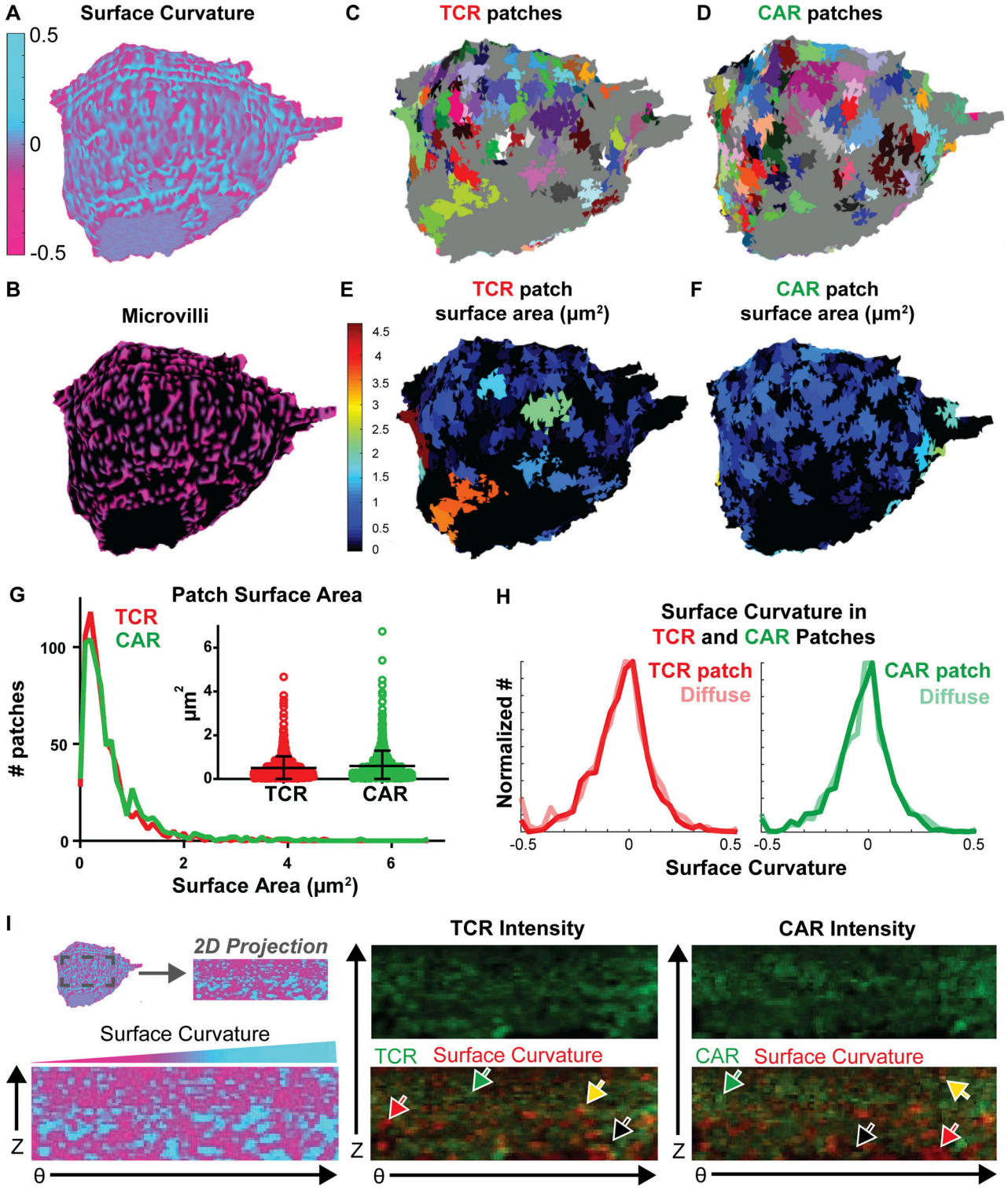

Figure 2. **Quantification of TCR and CAR patches relative to surface curvature. (A)** Curvature of the cell surface was mapped based off the cell boundary defined by CD45, with valleys marked by cyan and tips marked by magenta. Fixed CAR T cell was labeled with antibodies to MYC (CAR)-Alexa488, TCR (OKT3)-APC, and CD45-Alexa594. **(B)** MV are highlighted by masking the surface curvature in A based on convexity. **(C–F)** TCR (C and E) and CAR (D and F) clusters defined by regions of high local (3D) intensity are shown as different colors (C and D) and colored according to surface area of cluster (E and F). **(G)** Histogram and dot plot (inset) of cluster surface area is shown for TCR and CAR. TCR and CAR median values are 0.34 and 0.38 μm², respectively. Data is compiled from three cells (n = 688, 717 patches). Dot plot shows mean and SD. **(H)** Histograms of surface curvature for TCR (left) and CAR (right) found in patches or outside of patches for a representative cell (n = 186, 201 patches). **(I)** 2D projections from the surface show curvature increasing from convex (magenta on left, black in overlay) to concave (cyan on left, red in overlay); TCR intensity (middle); and CAR intensity. Yellow and red arrows mark membrane valleys with high and low receptor intensity, respectively. Green and black arrows mark membrane peaks with high and low receptor intensity, respectively.

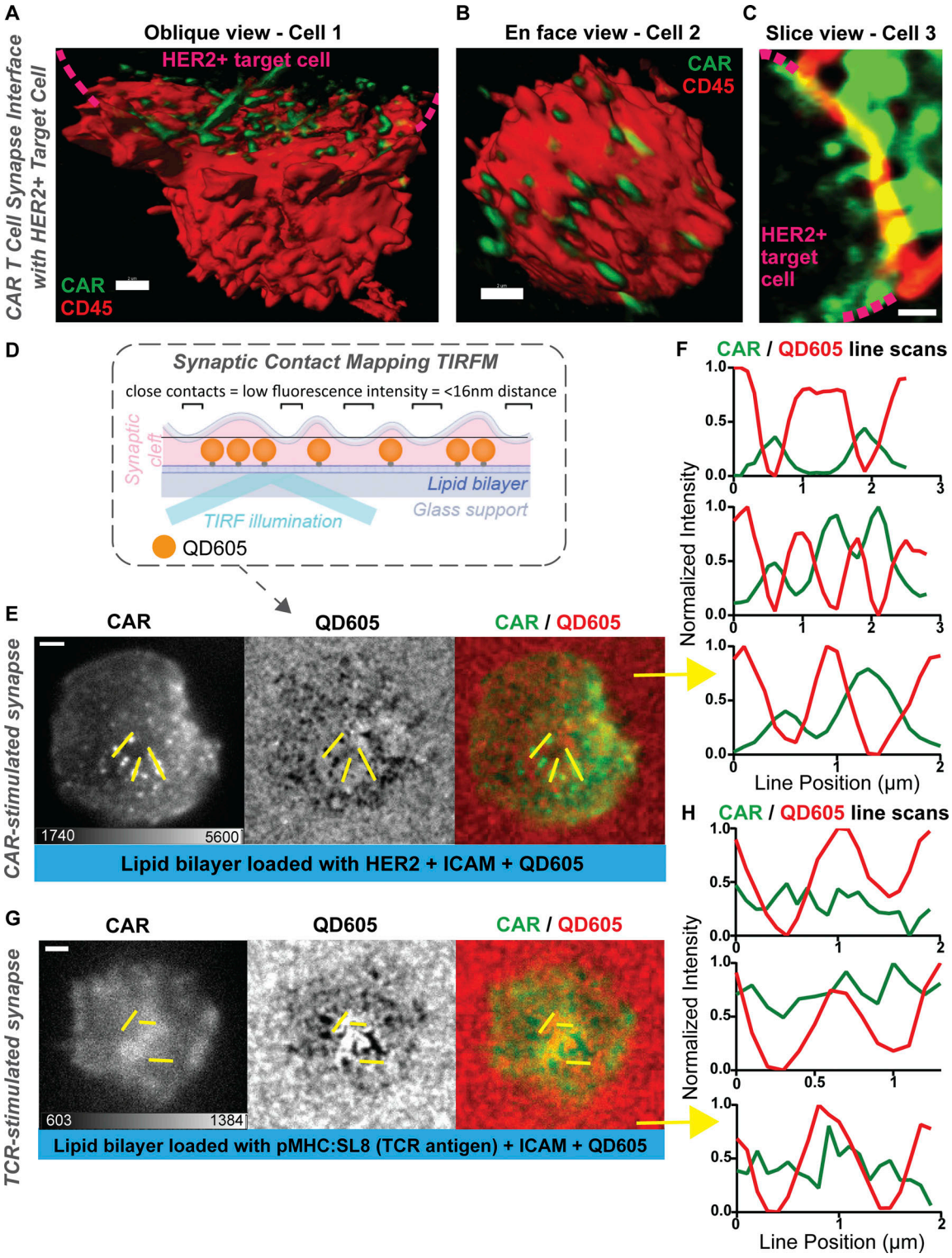

Figure 3. **CAR is enriched at sites of microvilli close contacts in synapses with cognate antigen, but not following engagement of endogenous TCR.** **(A–C)** Three examples of anti-HER2 CAR T cells interacting with HER2+ SKBR3 are shown from an oblique view of the synapse interface (A, Imaris normal shading mode, scale bar = 2 µm), en face synapse view (B, Imaris normal shading mode, scale bar = 2 µm), and a single *z*-slice (C, scale bar = 1 µm). The SKBR3 target cell location is marked by dashed magenta lines (A and C). Human CD8⁺ T cell expressing anti-HER2 CAR (4D5) was labeled with antibodies to MYC (CAR)-Alexa488 and CD45-Alexa647. **(D)** Schematic of synaptic contact mapping method. Lipid bilayer on glass support is loaded with Qdot 605, which is a red-fluorescent probe that occupies ~16 nm in height. Areas where the cell makes a close contact (<16 nm distance) appear as holes in the QD605 signal. **(E)** CAR T cell synapse imaged by TIRF showing CAR-mEmerald, MV projections (as seen by holes in QD605 signal), and overlay. Human CD8⁺ T cell expressing anti-HER2 CAR (mut4D5) interacting with lipid bilayer loaded with 625 ng HER2 + ICAM + QD605. Scale bar = 2 µm. **(F)** Line scans from E show anti-correlation of CAR-mEmerald and QD605, indicating enrichment of CARs within MV contacts. **(G)** OT-I mouse T cells were retrovirally transduced with anti-HER2 CAR

(mutCD45). Synapse shown was formed on lipid bilayer loaded with pMHC:SL8 + ICAM + QD605. TIRF imaging of CAR-mEmerald, QD605, and overlay are shown. Scale bar = 2 µm. **(H)** Line scans from G showing the lack of enrichment in CAR signal within QD605 holes, indicating that CAR microclusters do not accumulate in MV close contacts in absence of the CAR's cognate antigen.

differences (Fig. S4 D). Therefore, we found that a monomerized LA CAR supported the formation of synapse architectures and dynamics characteristic of TCRs on antigen-loaded SLBs, whereas HA dimerized CARs did not. Importantly, whereas TCR-mediated interactions are stabilized by signaling to LFA-1, CARs do not efficiently engage LFA-1 or form the typical adhesion ring (Davenport et al., 2018; Burton et al., 2022) visualized by confocal microscopy. Thus, the stability rendered by CARs is even more reliant upon the antigen receptor binding itself, further underlining the apparently overabundant strength of CAR scFv-antigen binding.

Given these proximal effects on IS dynamics, we sought to determine the downstream effects of the hyper-stable or more physiological receptors. To compare between HER2 levels for T cell stimulation experiments, we first used two breast cancer cell lines: the MCF7 luminal breast cancer cell line, which does not over-express HER2 (Comsa et al., 2015), and the SKBR3 cell line, which endogenously over-expresses HER2 and thus mirrors HER2-positive breast cancers (Mota et al., 2017; Fig. 5 E, Fig. S3 A, and Fig. S5 A). All combinations yielded robust T cell/target coupling (Friedman et al., 2006), and staining for early activation (CD69) and entry into cell cycle (Ki67) were similarly robust across conditions (Fig. S5, B–H). While all conditions induced a proliferative burst, rounds of proliferation varied significantly, with the greatest proliferation observed using LA dimeric CAR (Fig. 5, F and G).

Assaying effector function by intracellular staining for IFN-γ also revealed increased production of this cytokine in cells bearing LA CAR dimers relative to HA ones (Fig. 5 H). In these co-cultures, less IFN-γ was produced by dimeric CAR T cells when incubated with high-HER2 SKBR3s than with low-HER2 MCF7s. In this regard, while the LA monomer displayed a decreased magnitude of response, likely in part due to a lack of constitutively paired intracellular CD3ζ, it improved the expected dose-dependent response pattern. Thus, extracellular binding dynamics are likely translated to function as part of a careful balance between intracellular actin dynamics (Colin-York et al., 2019) and signaling efficiency (Harris et al., 2018; Gudipati et al., 2020; Salter et al., 2021).

Finally, we incubated mouse CAR T cells with MC38 tumor cells expressing variable HER2 levels—using this strategy to also minimize the effects of comparing between different target cell lines. LA and HA receptors performed similarly for cytokine production (Fig. S5, I and J), but when we shifted these cultures to hypoxia, mimicking the tumor microenvironment and licensing deeper progression into exhaustion (Scharping et al., 2021), the conventional HA dimer was more susceptible to exhaustion as measured by TOX and PD1 co-expression (Fig. 5 I), in line with recent work (Shakiba et al., 2022) using native TCRs.

In this work, we use LLS imaging to show that CARs and TCRs distribute as patches on isolated T cells, although not obligately overlapping in position. The independent segregation of CAR patches is likely due to differential miscibility and recruitment of membrane lipids related to combinations of transmembrane and cytoplasmic domains, although studies of this represent a significant tangent from our work. Future studies are needed to reveal the regulators of patch formation and to classify these features. Given the allowance for variable-sized patches used in this analysis, the patches we refer to may encompass multiple types of accumulations, such as from "condensates" (Lyon et al., 2021) or random fluctuations. Collectively, these features may heighten the T cell's sensitivity to antigen, with the appearance of a patch at a MV tip providing a means to "lock in" a signaling surface at the site of ligand engagement. Engagement of accessory receptors like LFA-1 (another means to "lock in") is critical to the function of natural TCRs, but notably, CAR stabilization is independent of those interactions (Davenport et al., 2018; Burton et al., 2022). Here, we use SCM TIRF imaging to show that CAR MCs accumulate at the tips of MV, which are hyperstabilized in comparison to those mediated by TCRs.

Multifocal IS and/or reduced actin velocity have been observed for T:DC interactions (Leithner et al., 2021), during thymic negative selection (Richie et al., 2002), and in settings of slower receptor unbinding kinetics (Colin-York et al., 2019). Given these findings, it is tempting to speculate that multifocal patterns may be a general indicator of relatively "strong" contacts (Mossman et al., 2005), although the implications of that phenotype vary by context. We see here on SLBs that it represents a super-physiological outcome of ultra-high affinity/avidity binding that does not correlate with optimal effector function. Many prior works also demonstrate that increasing the antigen binding strength does not reliably predict the efficiency of T cell activation and ultimate effector function, both for natural TCR (Corse et al., 2010; McMahan et al., 2006; Kalergis et al., 2001; Schmid et al., 2010; Dushek et al., 2011; Hebeisen et al., 2013) and engineered CAR (Harris et al., 2018; Ghorashian et al., 2019; Park et al., 2017; Liu et al., 2015). Importantly, the LA monomer best reproduced the expected dose response to antigen. While the monomer's reduced magnitude of response may in part result from too-far reduced extracellular binding capacity, it seems at least as likely to result from the monomer's lack of paired CD3ζ domains. This important nuance reinforces the idea that each aspect of CAR design must be considered in relation to the full molecular context rather than as an isolated feature which can be super-engineered for global application.

The biology underlying dynamic T cell MV likely shares much in common with interdigitating filopodia (Vasioukhin et al., 2000), podosomes (Murphy and Courtneidge, 2011; Kumari et al., 2015), and invadopodia (Murphy and Courtneidge, 2011; Sage et al., 2012). Future studies to characterize the regulators of T cell MV dynamics and better subclassify actin-based synaptic protrusions, especially those present during early synapses (studied here) vs. late synapses, will reveal new

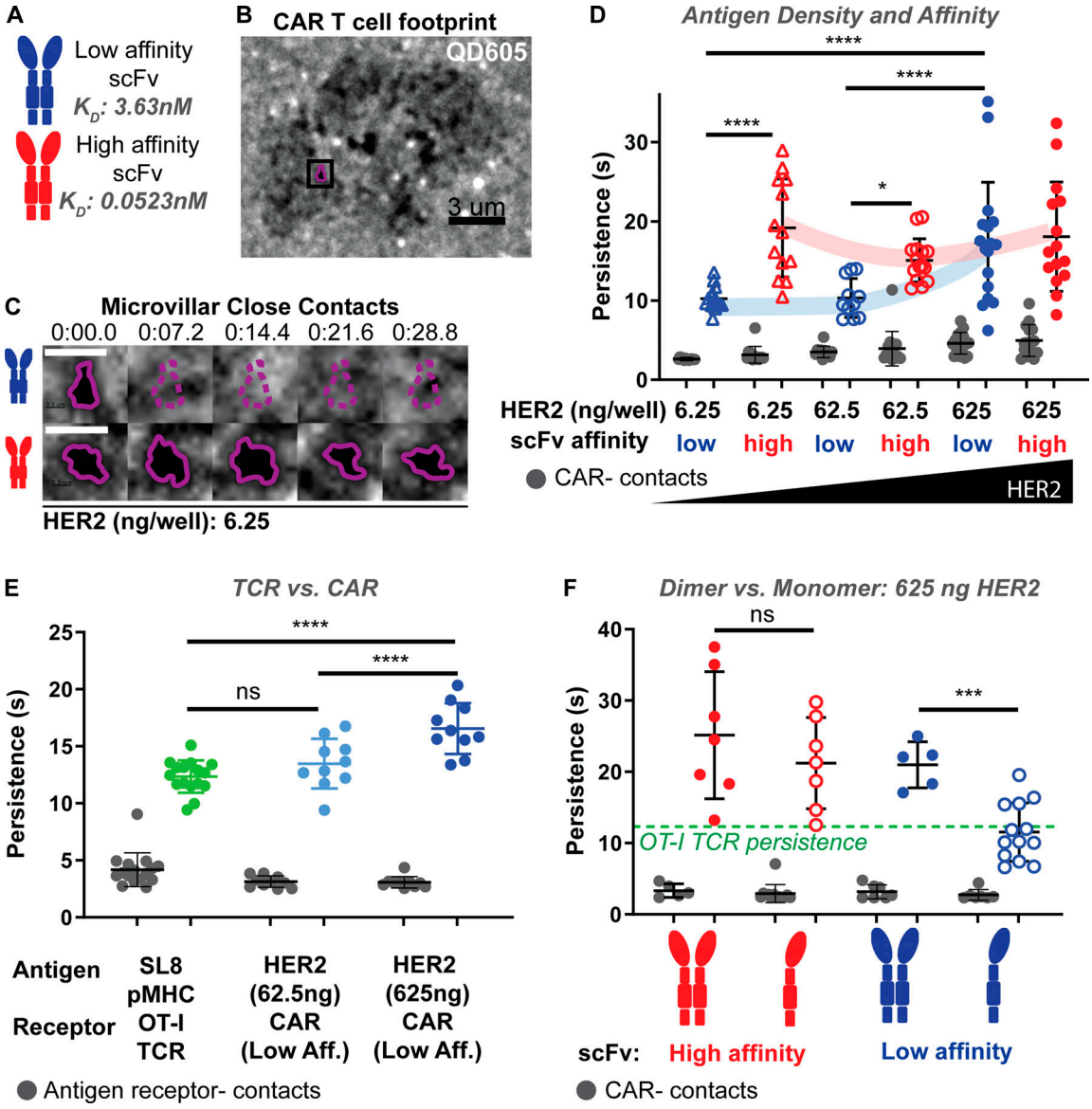

Figure 4. **Conventional CAR interactions of high affinity or high antigen density result in hyper-stabilization of underlying microvillar protrusion, which can be reduced using monomeric CAR. (A)** Experiments were performed comparing CARs with an HA scFv against HER2-based off trastuzumab (4D5, K_D = 0.0523 nM, red) and a lower affinity scFv made by substitution of three amino acids (see Table S1, mut4D5, K_D = 3.63 nM, blue). **(B)** Bilayers were loaded with fluorescent quantum dots (QD605) with a height of 16 nm. Locations where the cell makes close contact with the bilayer (<16 nm) are visualized as holes in QD605 signal due to their size-based exclusion. QD605 signal is shown for an LA CAR T cell interacting with a lipid bilayer loaded with 6.25 ng HER2. Outlined contact is shown in C. Scale bar = 3 µm. **(C)** QD605 signal across 5 time points are shown for the same field of view, each on low HER2 bilayers (6.25 ng/well). Top: Microvillus from LA CAR T cell moves out of view. Bottom: Microvillus from HA CAR T cell remains across time points. Scale bars = 1 µm. **(D)** CAR-occupied close contact persistence times (blue, red) and CAR-negative close contact persistence times (gray) are shown for varying antigen densities and affinities. All CAR:HER2 interactions tested result in CAR-occupied MV contact stabilization above background CAR-negative contacts (gray). Persistence time is further increased in interactions of HA CAR (red), even at lowest HER2 densities on the bilayer. For LA CAR (blue), only high levels of HER2 yield similar persistence times to high-affinity CAR. Data is shown for at least 11 cells per condition across four experiments (n = 13, 13, 11, 15, 17, 15 cells per group from left to right, respectively). **(E)** LA CAR was retrovirally expressed in primary mouse OT-I T cells. Receptor-occupied MV persistence times are shown for OT-I:SL8 (green), LA CAR:Low HER2 (light blue), and LA CAR:High HER2 (dark blue) interactions. All cognate interactions are stabilized above background receptor-negative contacts (gray). CAR:High HER2 persistence is hyper-stable relative to TCR:pMHC stabilization. Data is shown for at least 10 cells per condition across three experiments (n = 16, 10, 10 cells per group from left to right, respectively). **(F)** Dimers (filled dots) and monomers (open dots) are compared on high HER2 bilayers (625 ng/well). Only monomeric LA CAR regains natural persistence time of TCR:pMHC contacts (green dashed line). All receptor-occupied contacts are stabilized above non-cognate antigen interactions (gray). Data is shown for at least 5 cells per condition across three experiments (n = 7, 7, 5, 13 cells per group from left to right, respectively). **(D–F)** Error bars represent SD and analyses shown are Šídák's multiple comparisons tests.

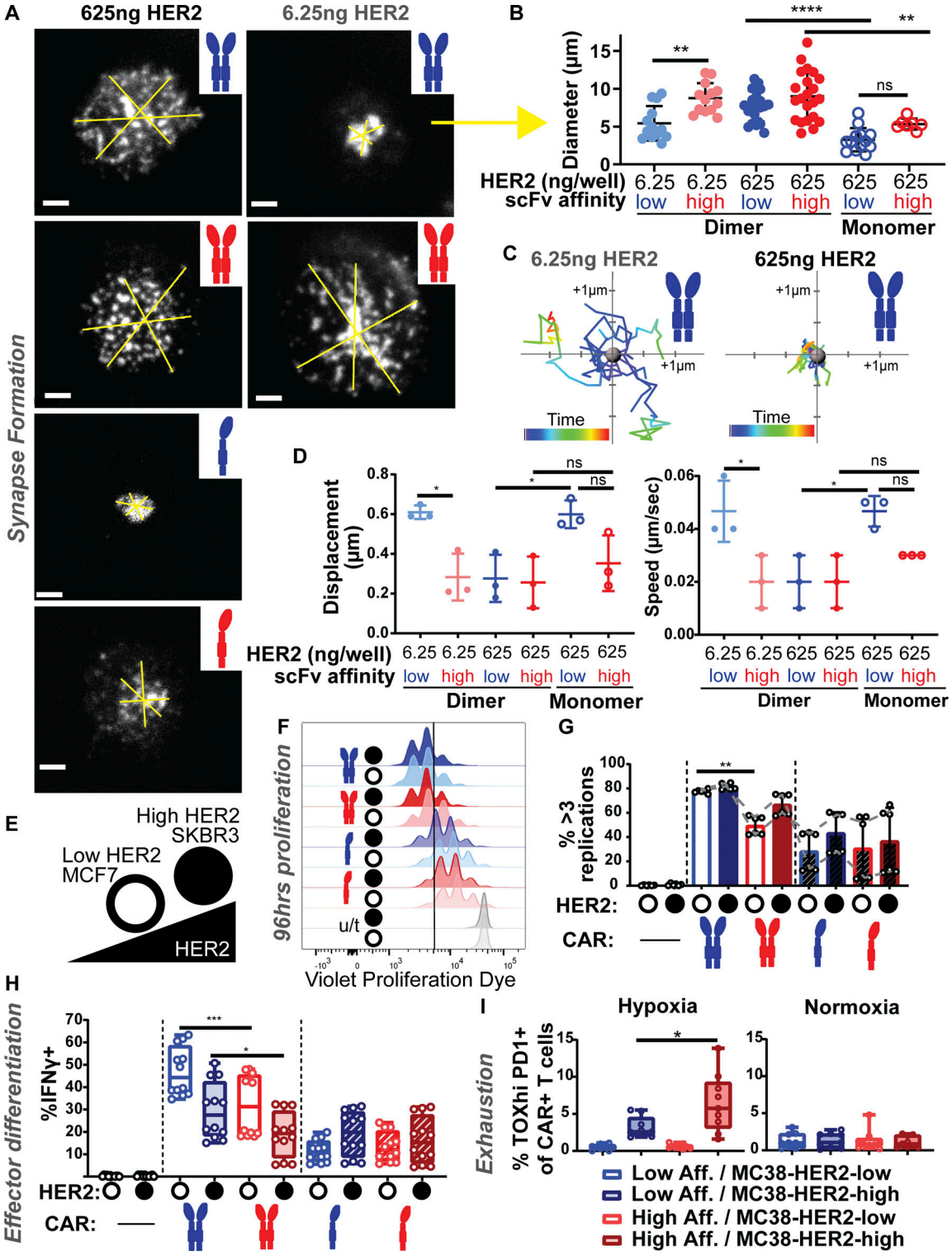

Figure 5. **Impaired movement of HA dimer CAR microclusters in synapses and reduced effector function. (A and B)** TIRF imaging of CAR-mEmerald is shown for synapses with LA or HA CAR interacting with low or high HER2-loaded bilayers (A). Time point shown is 93.6 s following the initiation of imaging, which began as synapses were starting to form. Yellow lines were drawn to span CAR microclusters in synapse, indicating diameter quantified in B. Three lines were averaged and line assignment was blinded to account for manual drawing. For dimeric CARs, only LA:low HER2 synapses result in accumulation of CAR microclusters at the center, indicated by lower diameter. Monomerization of CARs improves centralization on high HER2. Data is shown for at least 7 cells pooled from a minimum two independent experiments per condition (n = 13, 13, 20, 20, 13, 7 cells per group from left to right, respectively). Error bars represent SD. Analyses shown are Šídák's multiple comparisons tests. Scale bars = 2 μm. **(C and D)** Spots with tracking were assigned to CAR microclusters in Imaris. Examples of mobile (left, LA dimer on low HER2) and immobile (right, LA dimer on high HER2) microclusters are shown as a flower plot for 10 random tracks (C). Quantification is shown for the average displacement (left) and speed (right) of all CAR microclusters for a given cell (D, n = 3 cells per group, 30–294

tracks per cell). Limited mobility is apparent for dimeric CARs on high-HER2 loaded bilayers. On low-HER2 bilayers, LA CAR microclusters show increased mobility. Error bars represent SD. Analyses shown are Šídák's multiple comparisons tests. **(E)** Low HER2-expressing MCF7 (open circle) and high HER2-expressing SKBR3 (solid circle) cell lines were used to assess differences between HER2 levels in cell-cell interactions in vitro. **(F)** Proliferation is induced across all CAR+ conditions with low and high HER2, as seen by VPD dilution at 96 h following co-incubation. Line marks VPD dilution indicating at least 3 replication cycles (quantified in G). **(G)** Percentage of cells that have undergone at least 3 replication cycles. Replicates from two independent experiments of different donors are pooled (n = 6). Dashed lines indicate individual donor trends. Error bars represent SD. Analysis shown is Šídák's multiple comparisons test. **(H)** Intracellular staining with anti-IFN-γ-APC at 18 h following co-incubation. LA CAR induces greater IFN-γ than HA. Monomeric LA CAR has overall lower magnitude of response, but improves the dose response. Box and whiskers plot error bars showing minimum and maximum values (n = 12 samples per group pooled from four independent experiments and two donors). Analyses shown are Šídák's multiple comparisons tests. **(I)** LA (blue) and HA (red) CARs were retrovirally expressed in primary mouse CD8⁺ T cells and co-cultured with MC38 cells expressing low- or high-HER2 for 24 h in normoxia (20% oxygen) before separation into normoxic or hypoxic (1.5% oxygen) cultures for an additional 6 d. Hypoxic co-cultures of HA CAR T cells with MC38-HER2-high cells have significantly more TOX high/PD1+ cells than LA CAR T cells, indicative of development towards an exhausted state. Box and whiskers plot error bars showing minimum and maximum values (n = 9 samples pooled from three independent experiments). Analysis shown is unpaired t test.

mechanisms of control of T cell activation (Blumenthal and Burkhardt, 2020). Actin regulators like WASP are differentially engaged at protrusions depending on TCR signaling (Ditlev et al., 2019). Ultimately, specific nomenclature should be standardized. Here, we show that receptor binding affinity and avidity control the dynamics of synaptic MV. Given that MV persistence in TCR-occupied contacts is independent of signaling through ZAP70 (Cai et al., 2017), these findings indicate that affinity and avidity of binding directly affect the movements of opposing cell surfaces. This work opens up new avenues for future research to determine whether better quality T cells could be produced for cell therapies by boosting the intracellular signal downstream of physiologically normalized binding dynamics.

Materials and methods

Lentiviral and retroviral CAR constructs

All CARs were fused to C-terminal MYC tag, CD8α hinge/transmembrane domain, 4-1BB co-stimulatory domain, CD3ζ signaling domain, and an N-terminal mEmerald tag. Monomeric versions of each CAR were created using the Q5 Site Directed Mutagenesis Kit (#E0554S; NEB) yielding two cysteine to serine point mutations in the CD8α hinge (Hennecke and Cosson, 1993; Table S1).

Human T cell culture, lentiviral transduction, and co-incubations

Lenti-X 293T cells (Takara Bio) were transfected with pHR SIN including cloned transgene and packaging vectors pMD2.G and pCMVdR8.91 using TransIT-Lenti Transfection Reagent (#MIR6603; Mirus). On the day of transfection, primary human CD8⁺ T cells were thawed into complete human T cell media: X-VIVO 15 (#04-418Q; Lonza), 5% Human AB serum (#HP1022; Valley Biomedical) and 10 mM neutralized N-acetyl L-Cysteine (#A9165-25G; Sigma-Aldrich) supplemented with 30 U/ml recombinant human IL-2 (#202-IL; R&D Systems), and 55 µM beta-mercaptoethanol (#21985023; Thermo Fisher Scientific). The following day, Human T-Activator CD3/CD28 Dynabeads (#11161D; Thermo Fisher Scientific) were added at 1:1 ratio with thawed T cells. The next day, T cell media was replaced with Lenti-X 293T viral supernatant. For lentiviral transduction of monomeric CARs, virus was concentrated by PEG/NaCl precipitation, and stored at −80°C prior to use. Viral supernatant was replaced with fresh T cell media the next day, and T cells were allowed to recover for 1 d prior to Dynabead removal and sort. Cells were sorted for CAR-mEmerald expression in the range of 1-2 logs above background. Cells were then rested and used at 10–21 d post initial stimulation. Lenti-X 293T cells were cultured in Dulbecco's modified Eagle's medium (DMEM, #11995; Gibco) with 10% fetal bovine serum (MilliporeSigma), penicillin (50 U/ml) and streptomycin (50 µg/ml; #MP091670049; MP Biochemicals), and 1 mM sodium pyruvate (#S8636; Sigma-Aldrich). For early activation and intracellular cytokine assays, 5 × 10^4 T cells were added at a 1:1 ratio to 96-well flat-bottom plates with MCF7 (ATCC) or SKBR3 (ATCC) cells for 18 h. BD GolgiPlug (#555029) was added for the final 10 h. For proliferation assays, T cells were stained with Violet Proliferation Dye (#562158; BD) prior to plating of 2 × 10^4 T cells at 1:1 ratio with MCF7s or SKBR3s. Complete T cell media was supplemented the following day, and cells were analyzed by flow cytometry at 96 h following plating.

Flow cytometric analysis

Zombie NIR Fixable Viability Kit (#423106; BioLegend) was used for exclusion of dead cells. Surface staining was performed with anti-mouse Fc receptor antibody (clone 2.4G2, UCSF Hybridoma Core) or Human TruStain FcX (#422302; BioLegend) in PBS with 2% FCS for 30 min on ice. Table S2 lists all antibodies referenced for flow cytometry and imaging experiments. For experiments with staining of nuclear proteins, eBioscience Foxp3/Transcription Factor Staining Buffer Set (#00-5523-00; Thermo Fisher Scientific) was used for fixation and permeabilization. For all other experiments involving intracellular staining, BD Cytofix/Cytoperm (#554722) was used. Following fixation and permeabilization, cells were incubated with Fc block for 10 min on ice prior to addition of intracellular stain. Flow cytometry was performed on a BD Fortessa instrument, and sorting was performed on BD FACSAria or BD FACSAria Fusion instruments. FlowJo software (BD Biosciences) was used for all analyses.

Flow-cytometry-based coupling assay

MCF7 and SKBR3 cells expressing nuclear localization signal (NLS)-tagged mKate were incubated with anti-CD45-Alexa647-labelled T cells for 30 min in complete human T cell media. Samples were then spun down and resuspended in PBS with 2% FCS and DAPI for analysis with minimal pipetting to avoid dissociation of cell couples. Gating for coupling analysis was

performed by gating inclusively for singlets and doublets. Cells were then gated on DAPI$^-$, CD45$^+$, and CAR+ (or CAR– for untransduced controls). Percentage of these cells that are mKate+ was reported as T cells in doublets with tumor cells. Method was derived from previous work (Friedman et al., 2006).

Mice

C57BL/6J and B6.SJL-Ptprc^a Pepc^b/BoyJ (CD45.1) mice, used as sources of primary mouse T cells, were housed and bred at the University of California, San Francisco, according to Laboratory Animal Resource Center guidelines. Protocols were approved by the Institutional Animal Care and Use Committee of the University of California.

MC38-HER2 retroviral transduction

Truncated HER2, without intracellular signaling domains, (NP_004439.2; amino acids 1–730) was cloned into pIB2 retroviral vector. Phoenix cells were transfected using FuGENE 6 Transfection Reagent (#E2691; Promega), and retroviral supernatant was collected and used immediately for transfection of MC38s on days 2 and 3 following transfection. 2 d after the second transduction, cells were sorted for expression of HER2 (stained with anti-HER2-Alexa488). MC38-HER2 cells were then expanded and the retroviral transduction process was repeated. Following the second transduction, cells were then sorted into high-, medium-, and low-expression levels using MCF7 and SKBR3 cells as standards for low and high expression, respectively. MC38 cells were cultured in DMEM (#11995; Gibco) supplemented with 10% fetal bovine serum (Benchmark), 100 U/ml penicillin, 0.1 mg/ml streptomycin, 2 mM L-glutamine (#10378; Gibco), 10 mM HEPES (#15630106; Thermo Fisher Scientific), and 55 µM beta-mercaptoethanol (#21985023; Thermo Fisher Scientific).

Murine T cell culture, retroviral transduction, and functional assays

The mouse OT-I TCR system was chosen as a comparator to the anti-HER2 CAR for its affinity near the top of the common range, and in order to avoid double-transfection (of a human TCR along with a CAR) which otherwise would create significant experimental inefficiencies. For all experiments using murine T cells, cells were maintained in RPMI (#11875; Gibco) supplemented with 10% fetal bovine serum (Benchmark), 100 U/ml penicillin, 0.1 mg/ml streptomycin, 2 mM L-glutamine, 10 mM HEPES (#15630106; Thermo Fisher Scientific), 55 µM beta-mercaptoethanol (#21985023; Thermo Fisher Scientific), non-essential amino acids (#11140050; Thermo Fisher Scientific), 1 mM sodium pyruvate (#S8636; Sigma-Aldrich), and supplemented with 100 U/ml IL-2, which is referred to as complete RPMI. Single cell suspensions were prepared from the lymph nodes and spleens of C57BL/6J, *Ptprc^a* (CD45.1), or OT-I TCR transgenic mice. Following red blood cell lysis of splenocytes, negative selection using the EasySep Mouse T cell or CD8$^+$ T cell Isolation Kit (#19853; STEMCELL Technologies) was used to isolate CD8$^+$ T cells. T cells were activated in complete RPMI using CD3/CD28 Mouse T activator Dynabeads (#11-453-D; Thermo Fisher Scientific) for 24 h before the first round of retroviral transduction. For retrovirus production, Platinum-E cells were transfected with pMIG including CAR transgene using FuGene. Transfections were performed in DMEM (#11995; Gibco) supplemented with 10% fetal bovine serum (Benchmark) and 10 mM HEPES (#15630106; Thermo Fisher Scientific), which was replaced with complete RPMI (without IL-2) the following day. Retroviral supernatants were harvested at day 2 and 3 and stored in −80°C. Platinum-E cells were maintained in DMEM (#11995; Gibco) supplemented with 10% fetal bovine serum (Benchmark), 100 U/ml penicillin, 0.1 mg/ml streptomycin, 2 mM L-glutamine (#10378; Gibco), 10 mM HEPES (#15630106; Thermo Fisher Scientific), 10 µg/ml blasticidin (#A1113903; Thermo Fisher Scientific), and 1 µg/ml puromycin (#A1113803; Gibco). For T cell retroviral transduction, retroviral supernatant was added to T cells in retronectin-coated plates at 24 and 48 h following initial stimulation, and the plates were centrifuged for 1 h at 2,000 *g* and 30°C. After the second spinfection, cells were rested 2 d prior to Dynabead removal (4 d post-stim). T cells were then sorted for imaging or rested for an additional 6–7 d in 10 ng/ml recombinant murine IL-7 (#217-17; PeproTech) and 100 U/ml IL-2 and used for in vitro co-culture experiments. For binned HER2 expression level experiments, MC38-HER2 lines were sorted into five consecutive bins by HER2 expression using MCF7s and SKBR3s as the low and high HER2 standards, respectively. MC38-HER2 cells, sorted as described, were then plated at 5 × 10^4 cells/well in flat-bottom 96 well plates, and 5 × 10^4 T cells were then added, bringing the total volume to 200 µl/well complete RPMI. For hypoxia experiments, T cells were rested 6 d and then plated at 5 × 10^4 cells at a 1:1 ratio with MC38-HER2-high or MC38-HER2-low cells in two 96-well plates in complete RPMI. At 24 h, wells were replenished with complete RPMI + IL-2, and 5 × 10^4 MC38-HER2-high and -low cells were added. One plate was moved to 1.5% oxygen while the second was maintained at 20% oxygen. MC38-HER2-high and -low cells and media + IL-2 were then replenished every 2 d until analysis on day 7 after start of co-culture (6 d in hypoxia).

Surface plasmon resonance affinity measurements

Measurements were taken using a Biacore T200 instrument with CM4 sensor chip and HBs-EP + buffer. HER2-mIgG2aFc (#HE2-H5255; ACROBiosystems) was captured using anti-mIgG (50 RUs). Association and dissociation times were 120 and 900 s, respectively. Concentrations of scFv used for single cycle kinetics analysis: 0.33, 1, 3, 9, 27 nM.

Lattice light-sheet microscopy

5 mm round coverslips were cleaned by a plasma cleaner and coated with 2 µg/ml fibronectin in PBS at 37°C for 1 h, or at 4°C overnight, before use. ∼3 × 10^5 CAR T cells were loaded onto the coverslip and incubated at 37°C for 30 min. Cells were then fixed in d_2h_20 with 20 mM HEPES (#15630106; Thermo Fisher Scientific), 0.2 M sucrose (RPI #S240600, 4% paraformaldehyde (#15710; Election Microscopy Sciences), and 8% glut-aldehyde (#16019; Election Microscopy Sciences) for 10 min at room temperature. Coverslip was washed gently in 1 ml PBS and then stained with antibodies to CD45 and/or MYC with anti-mouse Fc receptor antibody (clone 2.4G2, UCSF Hybridoma Core).

Samples were stained for at least 30 min and kept at 4°C until use. Prior to imaging, coverslip was gently washed with 1 ml warmed RPMI without phenol red (#11835; Gibco) supplemented with 2% fetal bovine serum, 100 U/ml penicillin, 0.1 mg/ml streptomycin, 2 mM L-glutamine, 10 mM HEPES, and 50 µM β-mercaptoethanol (imaging media). For imaging of live CAR T cell interactions with MCF7 and SKBR3 targets, MCF7 or SKBR3 cells were plated onto fibronectin-coated coverslips 1–2 d prior to imaging, or onto Cell-Tak (#354240; Corning) coated coverslips with a 10 min spin at 1,400 rpm and 4°C. CAR T cells were stained with antibody to CD45-Alexa647 for 30 min on ice. Target cells on coverslip were stained with CFSE (#C34554; Invitrogen) for 20 min at 37°C, or were identified by nuclear-localized mKate expression. Cells were then washed and T cells were added onto the coverslip prior to being loaded into the sample bath with warmed imaging media and secured. Imaging was performed at 37°C with a 488, 560, or 642 nm laser (MPBC) dependent upon sample labeling. Exposure time was 10 ms per frame leading to a temporal resolution of ∼4.5 and ∼6.75 s in two- and three-color mode, respectively. LLS microscope was a homebuilt clone of the scope described by Chen et al. (2014) with a Nikon CFI Apo LWD 25× W 1.1 NA 2 mm working distance objective, Hamamatsu Orca Flash 4.0 v2 camera, and Custom LabView acquisition software. Method was derived from previous work (Cai et al., 2017).

Supported lipid bilayers, synaptic contact mapping, and calcium flux imaging

Preparation and use of supported lipid bilayers was performed as described previously (Cai et al., 2017; Beemiller et al., 2012b). Mixtures of 96.5% POPC, 2% DGS-NTA (Ni), 1% Biotinyl-Cap-PE and 0.5% PEG5,000-PE (#850457C, 790404C, 870273C, 880230C; Avanti Polar Lipids) were made in a round bottom flask and dried under a stream of nitrogen and then overnight under vacuum. The phospholipids were then rehydrated at a total concentration of 4 mM in PBS for 1 h to create crude liposomes. Small, unilamellar liposomes were then made by extruding through 100 nm Track Etch filter papers (#800309; Whatman) with an Avestin LiposoFast Extruder (Avestin).8-well Nunc Lab-Tek II chambered coverglass (#155360; Thermo Fisher Scientific) were cleaned by submersion in 5% Hellmanex III (#Z805939; Sigma-Aldrich). Flask containing chamber in solution was microwaved for 25 s and then allowed to clean at room temperature overnight. The chambers were then washed repeatedly with 18 Milli-Q water and then dried. Finally, 250 µl 3 M NaOH was added to each well for 15 min at 55°C. Wells were washed with 300 µl Milli-Q water and the NaOH cleaning was repeated. Wells were then washed thoroughly and dried prior to use. Lipid bilayers were set up on the chambered coverglass by adding 0.25 ml of a 0.4 mM liposome solution to the wells. After 30 min, wells were rinsed with 8 ml of PBS by repeated addition of 0.5 ml of PBS, then aspiration of 0.5 ml of the overlay. Non-specific binding sites were then blocked with 1% BSA in PBS for 30 min. After blocking, 25 ng of unlabeled streptavidin (#43-4301; Invitrogen) was added to each well and allowed to bind to bilayers for 30 min. After rinsing, protein mixes containing 63 ng recombinant human ICAM-1 (#AB151393; Abcam) and 6.25–625 ng biotinylated HER2 (#HE2-H822R; ACROBiosystems) or 6 ng pMHC in 2% BSA were injected into each well. pMHC was provided by the NIH Tetramer Facility. After binding for 30 min, wells were rinsed again and 25 ng of QDot605-streptavidin (#Q10101MP; Thermo Fisher Scientific) was added to each well. For calcium flux imaging, QDot605-streptavidin was not added. Bilayers were finally rinsed with imaging media before being heated to 37°C for experiments. Experiments using 5 µm diameter silica microspheres (#SS05003/SS05N; Bangs Laboratories) were performed as previously described (Beemiller et al., 2012a). Briefly, the same protocol was used for building a lipid bilayer on chamber coverglass as for 4×10^5 beads, based off equivalent surface area, but with washes performed by centrifugation instead of repeated aspiration. For synaptic contact mapping (SCM) experiments, 5×10^5 T cells were added to the well prior to imaging at 37°C in RPMI without phenol red (#11835; Gibco) supplemented with 2% fetal bovine serum, 100 U/ml penicillin, 0.1 mg/ml streptomycin, 2 mM L-glutamine, 10 mM HEPES, and 50 µM β-mercaptoethanol (imaging media). Once cells began interacting with the bilayer, imaging was initiated. For imaging of OT-I TCR, $1\text{-}2 \times 10^6$ OT-I T cells were stained with 2.5 µg H57-597 non-blocking monoclonal antibody conjugated to Alexa Fluor 488 on ice for 30 min, then rinsed once with complete imaging media. Imaging method for synaptic contact mapping was derived from previous work (Cai et al., 2017). The TIRF microscope is based on a Zeiss Axiovert 200 M equipped with a 100× 1.45NA oil immersion objective, DG-4 Xenon light source (Sutter) and Zeiss TIRF slider (Cai et al., 2017; Beemiller et al., 2012b). All images were collected using a DV2 image splitter (Photometrics) positioned in front of an Evolve EMCCD (Photometrics). A 4 band multi-color TIRF dichroic located in the microscope separated the excitation and emission light for imaging (Chroma Technology). Images of CAR or TCR were collected by imaging CAR-mEmerald (or Alexa Fluor 488-labeled TCRs) using TIRF mode, by imaging QD605-streptavidin in widefield mode, and by imaging cells with interference reflection microscopy (IRM), also in widefield mode. Widefield QD605-strepavidin images were collected using a 405/10 nm excitation filter (Chroma Technology) located in the DG4 light source, while samples imaged with TIRF were excited by an Obis 488 nm laser (Coherent). IRM images were acquired using a 635/20 nm excitation filter (Chroma Technology) positioned in the DG4 light source. The CAR/TCR and QD605 emitted fluorescence signals were separated using a DV2 image splitter with a 565 nm long-pass dichroic mirror installed along with 520/35 and 605/70 nm emission filters (Chroma). Images containing the IRM signal were acquired through the long-pass dichroic and 605/70 nm emission filter in the image splitter. For Fura-2 imaging, cells were stained with 2 µM Fura-2 dye (#F1221; Thermo Fisher Scientific) for 15 min at room temperature. Cells were then washed in imaging media, and 5×10^5 T cells were added to the imaging well. 3 min after addition of cells, acquisition was initiated. Fura-2 imaging experiments were acquired using a 40 × 1.3NA oil immersion objective (Zeiss) and the same light source and dichroic described above. Widefield Fura-2 340 and 380 nm images were collected using 340/26 (Semrock) and 380/30 (Chroma, VT) excitation filters,

respectively, located in the DG4 light source. MetaMorph Version 7.6.5.0 was used for data acquisition.

Image analysis

All computational image analysis for SCM imaging was performed in Matlab (The Mathworks), Imaris version 9.2.1 or 7.6.3 (Bitplane), and Fiji. CAR-mEmerald microcluster tracking analysis was performed using the spots function in Imaris with the following parameters: 0.25 µm estimated diameter, autoregressive motion tracking, 0.5 µm maximum distance, gap size 3, track duration >5 s. Centroid positions for dot product calculations were defined by making a surface of the synapse CAR-mEmerald interface in Imaris with grain size of 3 µm and largest sphere diameter of 1 µm. Analysis for LLS was performed in Imaris and Matlab. No gamma adjustments were applied. Unique analysis code has been made available through GitHub and can be found at the URLs included below.

Lattice light-sheet: Post processing

Raw data were deconvolved using the iterative Richardson-Lucy deconvolution process with a known point spread function that was recorded for each color prior to the experiment, as described previously (Cai et al., 2017). A typical sample area underwent 15-20 iterations of deconvolution. For live imaging experiments, photobleaching correction was applied in FIJI using the histogram matching method.

Close contact segmentation and persistence analysis

Close contact segmentation, CAR co-localization, and persistence time analysis was performed using Matlab and Imaris as previously described (Cai et al., 2017). Briefly, the IRM images were used to define the region of the cell interface. Active contour segmentation of the QD605 image was then used to define close contact regions. These regions were then converted to Spots objects in Imaris. CAR intensity was masked to regions of close contacts, and the average intensity for each contact area was then plotted in a histogram. A Gaussian distribution curve centered at the background fluorescence median was overlayed. Contacts that fell within 3 sigma of the Gaussian distribution were considered CAR^-, while the higher intensity contacts were considered CAR+. These contacts were then separated into separate image stacks and persistence time for individual contacts was calculated. Contact persistence time was determined by summing the number of frames each binary connected component object existed for and multiplying by the time per frame. Contacts were assumed to not travel more than their diameter per time point. Code for analysis of persistence times has been made available: https://github.com/BIDCatUCSF/NanocontactsTIRF_V5.

Radial intensity profiles

Definition of cell boundary, assignment of radial coordinates, and plotting of pixel intensities were performed using MatLab. The outer edge (boundary) of cells was detected using a custom program which primarily applied a two-step kmeans clustering calculation on each of the image slices collected in the z-stack of images describing a single cell. The boundary was then eroded by three pixels to accommodate the resolution of the LLS imaging system. Code for defining the cell boundary: https://github.com/BIDCatUCSF/Exterior-t-Cell-Edge-Detection.
Radial coordinates were assigned for plotting of radial intensity profiles using this code: https://github.com/BIDCatUCSF/Outer-Boundary-Profile-Code. Binned intensity was measured by taking a moving average of ten pixels. Excursions of the binned intensity above the channel mean intensity +3 SD were used as the threshold to define patches.

Three-dimensional surface curvature mapping and patch analysis

The surface curvature and patch analysis used here was performed in MatLab as described in Cai et al. 2022. Briefly, the cell boundaries (as defined above for radial intensity profiles) were used to calculate Pearson's correlation coefficients for variable sized kernels in three dimensions, roughly of the shape of the point spread function. These correlation coefficients were then used as the basis for clustering analysis by segmentation and watershed, creating the patches. Surface curvature was calculated for each position of the cell boundary, mapped by color, and thresholded to regions of low curvature to indicate peaks on the cell surface. Projections of the surface curvature and receptor intensity onto two dimensions were created using Map3-2D software (Sendra et al., 2015). Relative co-localization of TCR and CAR patches was assessed by counting the number of TCR and CAR patches that met varying thresholds of overlap with CAR and TCR patches, respectively.

Fura-2 ratio image analysis

Fura-2 340/380 nm ratio images were created in MetaMorph Version 7.6.5.0 using a maximum ratio of 7 and imported to Imaris for tracking using the surface function with the following parameters: 1 µm grain size, 0.75 µm diameter of largest sphere, 2 µm region growing estimated diameter autoregressive motion tracking, 2 µm maximum distance, gap size 1, track duration above 148 s. For analysis of final time point, surfaces were made for all cells in field of view without tracking: 0.75 µm grain size, 0.75 µm diameter of largest sphere, 1.5 µm region growing estimated diameter. Maximum 340/380 nm ratio per cell was compared for all cells in field of view at final imaging time point—5.5 min after addition of T cells to chamber well.

Statistics

Statistical tests were performed using GraphPad Prism Version 9.0.1. Independent experiments and donors are as noted in figure legends—all other replicates are technical replicates. Significance tests are as described in legends and include: Tukey's multiple comparisons tests, Šídák's multiple comparisons tests, and two-tailed *t* tests. Data distribution was assumed to be normal, but this was not formally tested. Scatter plots show mean and SD (error bars). Box and whisker plots indicate median, 25th to 75th percentile (box), and minimum to maximum (whiskers). P values are reported as follows: ≥ 0.05 as ns, 0.01–0.05 as *, 0.001–0.01 as **, 0.0001–0.001 as ***, and < 0.0001 as ****.

Online supplemental material

Fig. S1 shows imaging of TCR and CAR on the surface of isolated T cells. Fig. S2 shows imaging of CAR T cell:target interactions. Fig. S3 shows CAR T cell calcium flux and close contact fluorescence. Fig. S4 shows CAR microcluster dynamics. Fig. S5 shows effects of CAR affinity, antigen density, and monomerization on CAR T cell activity. Video 1 shows LLS imaging of anti-HER2 CAR T cell. Video 2 shows LLS live cell imaging of anti-HER2 CAR T cell in synapse with HER2+ SKBR3 cell. Video 3 shows individual close contacts imaged by SCM TIRF microscopy. Video 4 shows Fura-2 calcium flux imaging of LA and HA CAR T cells on low- and high-HER2 bilayers. Video 5 shows CAR microcluster tracking analysis—LA dimer on low HER2 bilayer. Video 6 shows CAR microcluster tracking analysis—HA dimer on low HER2 bilayer. Video 7 shows CAR microcluster tracking analysis—LA dimer on high HER2 bilayer. Video 8 shows CAR microcluster tracking analysis—HA dimer on high HER2 bilayer. Video 9 shows CAR microcluster tracking analysis—LA monomer on high HER2 bilayer. Video 10 shows CAR microcluster tracking analysis—HA monomer on high HER2 bilayer. Table S1 lists mutations in CAR scFv (mutCD45) and CD8α hinge/TMD (monomer). Table S2 lists antibodies referenced for flow cytometry and imaging experiments.

Data availability

The datasets and unique materials generated during the current study are available from the corresponding author on reasonable request. Unique analysis codes have been made available and can be accessed through the GitHub links provided in the relevant Materials and methods sections.

Acknowledgments

We thank the Krummel and Roybal labs and the Biological Imaging Development CoLab for valuable discussions, and Erron Titus for critical reading. We acknowledge the Parnassus Flow Cytometry CoLab (RRID:SCR_018206) for assistance generating flow cytometry data.

Funding to M.F. Krummel: NIH R01 AI052116 and Sandler Program for Breakthrough Biomedical Research (UCSF).

Author contributions: C. Beppler designed, conducted, and analyzed most experiments, and drafted the manuscript. J. Eichorst and K. Marchuk authored unique MatLab codes and discussed data. K. Marchuk also assisted with LLS imaging acquisition. E. Cai discussed project design. C.A. Castellanos assisted with experiments and discussed data. V. Sriram designed affinity measurement experiments. K.T. Roybal contributed to the formulation of the project, designed experiments, provided reagents for experiments involving human T cells, and interpreted data. M.F. Krummel contributed to the formulation of the project, designed experiments, interpreted data, and developed the manuscript. All authors contributed manuscript revisions.

Disclosures: V. Sriram reported other from Pionyr Immunotherapeutics outside the submitted work. No other disclosures were reported.

Submitted: 26 May 2022
Revised: 25 October 2022
Accepted: 29 November 2022

References

Aramesh, M., D. Stoycheva, I. Sandu, S.J. Ihle, T. Zünd, J.Y. Shiu, C. Forró, M. Asghari, M. Bernero, S. Lickert, et al. 2021. Nanoconfinement of microvilli alters gene expression and boosts T cell activation. *Proc. Natl. Acad. Sci. USA*. 118:e2107535118. https://doi.org/10.1073/pnas.2107535118

Beemiller, P., J. Jacobelli, and M. Krummel. 2012a. Imaging and analysis of OT1 T cell activation on lipid bilayers. *Protoc. Exch.* https://doi.org/10.1038/protex.2012.028

Beemiller, P., J. Jacobelli, and M.F. Krummel. 2012b. Integration of the movement of signaling microclusters with cellular motility in immunological synapses. *Nat. Immunol.* 13:787–795. https://doi.org/10.1038/ni.2364

Blichfeldt, E., L.A. Munthe, J.S. Røtnes, and B. Bogen. 1996. Dual T cell receptor T cells have a decreased sensitivity to physiological ligands due to reduced density of each T cell receptor. *Eur. J. Immunol.* 26:2876–2884. https://doi.org/10.1002/eji.1830261211

Blumenthal, D., and J.K. Burkhardt. 2020. Multiple actin networks coordinate mechanotransduction at the immunological synapse. *J. Cell Biol.* 219:e201911058. https://doi.org/10.1083/jcb.201911058

Brameshuber, M., F. Kellner, B.K. Rossboth, H. Ta, K. Alge, E. Sevcsik, J. Göhring, M. Axmann, F. Baumgart, N.R.J. Gascoigne, et al. 2018. Monomeric TCRs drive T cell antigen recognition. *Nat. Immunol.* 19:487–496. https://doi.org/10.1038/s41590-018-0092-4

Brentjens, R.J., M.L. Davila, I. Riviere, J. Park, X. Wang, L.G. Cowell, S. Bartido, J. Stefanski, C. Taylor, M. Olszewska, et al. 2013. CD19-targeted T cells rapidly induce molecular remissions in adults with chemotherapy-refractory acute lymphoblastic leukemia. *Sci. Transl. Med.* 5:177ra38. https://doi.org/10.1126/scitranslmed.3005930

Burton, J., J.A. Siller-Farfán, J. Pettmann, B. Salzer, M. Kutuzov, P.A. van der Merwe, and O. Dushek. 2022. Inefficient exploitation of accessory receptors reduces the sensitivity of chimeric antigen receptors. *bioRxiv*. (Preprint posted February 09, 2022). https://doi.org/10.1101/2021.10.26.465853

Cai, E., C. Beppler, J. Eichorst, K. Marchuk, S.W. Eastman, and M.F. Krummel. 2022. T cells use distinct topographical and membrane receptor scanning strategies that individually coalesce during receptor recognition. *Proc. Natl. Acad. Sci. USA*. 119:e2203247119. https://doi.org/10.1073/pnas.2203247119

Cai, E., K. Marchuk, P. Beemiller, C. Beppler, M.G. Rubashkin, V.M. Weaver, A. Gerard, T.-L. Liu, B.-C. Chen, E. Betzig, et al. 2017. Visualizing dynamic microvillar search and stabilization during ligand detection by T cells. *Science*. 356:eaal3118. https://doi.org/10.1126/science.aal3118

Campi, G., R. Varma, and M.L. Dustin. 2005. Actin and agonist MHC-peptide complex-dependent T cell receptor microclusters as scaffolds for signaling. *J. Exp. Med.* 202:1031–1036. https://doi.org/10.1084/jem.20051182

Chen, B.-C., W.R. Legant, K. Wang, L. Shao, D.E. Milkie, M.W. Davidson, C. Janetopoulos, X.S. Wu, J.A. Hammer, Z. Liu, et al. 2014. Lattice light-sheet microscopy: Imaging molecules to embryos at high spatiotemporal resolution. *Science*. 346:1257998. https://doi.org/10.1126/science.1257998

Colin-York, H., Y. Javanmardi, M. Skamrahl, S. Kumari, V.T. Chang, S. Khuon, A. Taylor, T.L. Chew, E. Betzig, E. Moeendarbary, et al. 2019. Cytoskeletal control of antigen-dependent T cell activation. *Cell Rep.* 26:3369–3379.e5. https://doi.org/10.1016/j.celrep.2019.02.074

Comsa, Ş., A.M. Cimpean, and M. Raica. 2015. The story of MCF-7 breast cancer cell line: 40 years of experience in research. *Anticancer Res.* 35:3147–3154

Corse, E., R.A. Gottschalk, M. Krogsgaard, and J.P. Allison. 2010. Attenuated T cell responses to a high-potency ligand in vivo. *PLoS Biol.* 8:e1000481. https://doi.org/10.1371/journal.pbio.1000481

Davenport, A.J., R.S. Cross, K.A. Watson, Y. Liao, W. Shi, H.M. Prince, P.A. Beavis, J.A. Trapani, M.H. Kershaw, D.S. Ritchie, et al. 2018. Chimeric antigen receptor T cells form nonclassical and potent immune synapses driving rapid cytotoxicity. *Proc. Natl. Acad. Sci. USA*. 115:E2068–E2076. https://doi.org/10.1073/pnas.1716266115

Ditlev, J.A., A.R. Vega, D.V. Köster, X. Su, T. Tani, A.M. Lakoduk, R.D. Vale, S. Mayor, K. Jaqaman, and M.K. Rosen. 2019. A composition-dependent

molecular clutch between T cell signaling condensates and actin. *Elife*. 8:e42695. https://doi.org/10.7554/eLife.42695

Dushek, O., M. Aleksic, R.J. Wheeler, H. Zhang, S.P. Cordoba, Y.C. Peng, J.L. Chen, V. Cerundolo, T. Dong, D. Coombs, and P.A. van der Merwe. 2011. Antigen potency and maximal efficacy reveal a mechanism of efficient T cell activation. *Sci. Signal.* 4:ra39. https://doi.org/10.1126/scisignal.2001430

Farrell, M.V., S. Webster, K. Gaus, and J. Goyette. 2020. T cell membrane heterogeneity aids antigen recognition and T cell activation. *Front. Cell Dev. Biol.* 8:609. https://doi.org/10.3389/fcell.2020.00609

Friedl, P., A.T. den Boer, and M. Gunzer. 2005. Tuning immune responses: Diversity and adaptation of the immunological synapse. *Nat. Rev. Immunol.* 5:532–545. https://doi.org/10.1038/nri1647

Friedman, R.S., P. Beemiller, C.M. Sorensen, J. Jacobelli, and M.F. Krummel. 2010. Real-time analysis of T cell receptors in naive cells in vitro and in vivo reveals flexibility in synapse and signaling dynamics. *J. Exp. Med.* 207:2733–2749. https://doi.org/10.1084/jem.20091201

Friedman, R.S., J. Jacobelli, and M.F. Krummel. 2006. Surface-bound chemokines capture and prime T cells for synapse formation. *Nat. Immunol.* 7:1101–1108. https://doi.org/10.1038/ni1384

Garcia, K.C., C.A. Scott, A. Brunmark, F.R. Carbonet, P.A. Peterson, I.A. Wilson, and L. Teyton. 1996. CD8 enhances formation of stable T-cell receptor/MHC class I molecule complexes. *Nature*. 384:577–581. https://doi.org/10.1038/384577a0

Ghorashian, S., A.M. Kramer, S. Onuoha, G. Wright, J. Bartram, R. Richardson, S.J. Albon, J. Casanovas-Company, F. Castro, B. Popova, et al. 2019. Enhanced CAR T cell expansion and prolonged persistence in pediatric patients with ALL treated with a low-affinity CD19 CAR. *Nat. Med.* 25:1408–1414. https://doi.org/10.1038/s41591-019-0549-5

Grakoui, A., S.K. Bromley, C. Sumen, M.M. Davis, A.S. Shaw, P.M. Allen, and M.L. Dustin. 1999. The immunological synapse : A molecular machine controlling T cell activation. *Science*. 285:221–227. https://doi.org/10.1126/science.285.5425.221

Gudipati, V., J. Rydzek, I. Doel-Perez, V.D.R. Gonçalves, L. Scharf, S. Königsberger, E. Lobner, R. Kunert, H. Einsele, H. Stockinger, et al. 2020. Inefficient CAR-proximal signaling blunts antigen sensitivity. *Nat. Immunol.* 21:848–856. https://doi.org/10.1038/s41590-020-0719-0

Harris, D.T., M.V. Hager, S.N. Smith, Q. Cai, J.D. Stone, P. Kruger, M. Lever, O. Dushek, T.M. Schmitt, P.D. Greenberg, and D.M. Kranz. 2018. Comparison of T Cell activities mediated by human TCRs and CARs that use the same recognition domains. *J. Immunol.* 200:1088–1100. https://doi.org/10.4049/jimmunol.1700236

Hebeisen, M., L. Baitsch, D. Presotto, P. Baumgaertner, P. Romero, O. Michielin, D.E. Speiser, and N. Rufer. 2013. SHP-1 phosphatase activity counteracts increased T cell receptor affinity. *J. Clin. Invest.* 123:1044–1056. https://doi.org/10.1172/JCI65325

Hennecke, S., and P. Cosson. 1993. Role of transmembrane domains in assembly and intracellular transport of the CD8 molecule. *J. Biol. Chem.* 268:26607–26612. https://doi.org/10.1016/S0021-9258(19)74355-5

Hu, Y.S., H. Cang, and B.F. Lillemeier. 2016. Superresolution imaging reveals nanometer- and micrometer-scale spatial distributions of T-cell receptors in lymph nodes. *Proc. Natl. Acad. Sci. USA*. 113:7201–7206. https://doi.org/10.1073/pnas.1512331113

Jung, Y., I. Riven, S.W. Feigelson, E. Kartvelishvily, K. Tohya, M. Miyasaka, R. Alon, and G. Haran. 2016. Three-dimensional localization of T-cell receptors in relation to microvilli using a combination of superresolution microscopies. *Proc. Natl. Acad. Sci. USA*. 113:E5916–E5924. https://doi.org/10.1073/pnas.1605399113

Kalergis, A.M., N. Boucheron, M.A. Doucey, E. Palmieri, E.C. Goyarts, Z. Vegh, I.F. Luescher, and S.G. Nathenson. 2001. Efficient T cell activation requires an optimal dwell-time of interaction between the TCR and the pMHC complex. *Nat. Immunol.* 2:229–234. https://doi.org/10.1038/85286

Kalos, M., B.L. Levine, D.L. Porter, S. Katz, S.A. Grupp, A. Bagg, and C.H. June. 2011. T cells with chimeric antigen receptors have potent antitumor effects and can establish memory in patients with advanced leukemia. *Sci. Transl. Med.* 3:95ra73. https://doi.org/10.1126/scitranslmed.3002842

Kumar, R., M. Ferez, M. Swamy, I. Arechaga, M.T. Rejas, J.M. Valpuesta, W.W.A. Schamel, B. Alarcon, and H.M. van Santen. 2011. Increased sensitivity of antigen-experienced T cells through the enrichment of oligomeric T cell receptor complexes. *Immunity*. 35:375–387. https://doi.org/10.1016/j.immuni.2011.08.010

Kumari, S., D. Depoil, R. Martinelli, E. Judokusumo, G. Carmona, F.B. Gertler, L.C. Kam, C.V. Carman, J.K. Burkhardt, D.J. Irvine, and M.L. Dustin. 2015. Actin foci facilitate activation of the phospholipase C-γ in primary T lymphocytes via the WASP pathway. *Elife*. 4:e04953. https://doi.org/10.7554/eLife.04953

Labrecque, N., L.S. Whitfield, R. Obst, C. Waltzinger, C. Benoist, and D. Mathis. 2001. How much TCR does a T cell need? *Immunity*. 15:71–82. https://doi.org/10.1016/S1074-7613(01)00170-4

Leithner, A., L.M. Altenburger, R. Hauschild, F.P. Assen, K. Rottner, T.E.B. Stradal, A. Diz-Muñoz, J.V. Stein, and M. Sixt. 2021. Dendritic cell actin dynamics control contact duration and priming efficiency at the immunological synapse. *J. Cell Biol.* 220:e202006081. https://doi.org/10.1083/JCB.202006081

Lever, M., P.K. Maini, P.A. van der Merwe, and O. Dushek. 2014. Phenotypic models of T cell activation. *Nat. Rev. Immunol.* 14:619–629. https://doi.org/10.1038/nri3728

Lillemeier, B.F., J.R. Pfeiffer, Z. Surviladze, B.S. Wilson, and M.M. Davis. 2006. Plasma membrane-associated proteins are clustered into islands attached to the cytoskeleton. *Proc. Natl. Acad. Sci. USA*. 103:18992–18997. https://doi.org/10.1073/pnas.0609009103

Liu, X., S. Jiang, C. Fang, S. Yang, D. Olalere, E.C. Pequignot, A.P. Cogdill, N. Li, M. Ramones, B. Granda, et al. 2015. Affinity-tuned ErbB2 or EGFR chimeric antigen receptor T cells exhibit an increased therapeutic index against tumors in mice. *Cancer Res.* 75:3596–3607. https://doi.org/10.1158/0008-5472.CAN-15-0159

Lyon, A.S., W.B. Peeples, and M.K. Rosen. 2021. A framework for understanding the functions of biomolecular condensates across scales. *Nat. Rev. Mol. Cell Biol.* 22:215–235. https://doi.org/10.1038/s41580-020-00303-z

Maude, S.L., N. Frey, P.A. Shaw, R. Aplenc, D.M. Barrett, N.J. Bunin, A. Chew, V.E. Gonzalez, Z. Zheng, S.F. Lacey, et al. 2014. Chimeric antigen receptor T cells for sustained remissions in leukemia. *N. Engl. J. Med.* 371:1507–1517. https://doi.org/10.1056/nejmoa1407222

McMahan, R.H., J.A. McWilliams, K.R. Jordan, S.W. Dow, D.B. Wilson, and J.E. Slansky. 2006. Relating TCR-peptide-MHC affinity to immunogenicity for the design of tumor vaccines. *J. Clin. Invest.* 116:2543–2551. https://doi.org/10.1172/JCI26936

Monks, C.R., B.A. Freiberg, H. Kupfer, N. Sciaky, and A. Kupfer. 1998. Three-dimensional segregation of supramolecular activation clusters in T cells. *Nature*. 395:82–86. https://doi.org/10.1038/25764

Mossman, K.D., G. Campi, J.T. Groves, and M.L. Dustin. 2005. Altered TCR signaling from geometrically repatterned immunological synapses. *Science*. 310:1191–1193. https://doi.org/10.1126/science.1119238

Mota, A.L., A.F. Evangelista, T. Macedo, R. Oliveira, C. Scapulatempo-Neto, R.A. Vieira, and M.M.C. Marques. 2017. Molecular characterization of breast cancer cell lines by clinical immunohistochemical markers. *Oncol. Lett.* 13:4708–4712. https://doi.org/10.3892/ol.2017.6093

Murphy, D.A., and S.A. Courtneidge. 2011. The "ins" and "outs" of podosomes and invadopodia: Characteristics, formation and function. *Nat. Rev. Mol. Cell Biol.* 12:413–426. https://doi.org/10.1038/nrm3141

Orbach, R., and X. Su. 2020. Surfing on membrane waves: Microvilli, curved membranes, and immune signaling. *Front. Immunol.* 11:2187. https://doi.org/10.3389/fimmu.2020.02187

Park, S., E. Shevlin, Y. Vedvyas, M. Zaman, S. Park, Y.S. Hsu, I.M. Min, and M.M. Jin. 2017. Micromolar affinity CAR T cells to ICAM-1 achieves rapid tumor elimination while avoiding systemic toxicity. *Sci. Rep.* 7:14366. https://doi.org/10.1038/s41598-017-14749-3

Pettmann, J., A.M. Santos, O. Dushek, and S.J. Davis. 2018. Membrane ultrastructure and T cell activation. *Front. Immunol.* 9:2152. https://doi.org/10.3389/fimmu.2018.02152

Razvag, Y., Y. Neve-Oz, J. Sajman, M. Reches, and E. Sherman. 2018. Nanoscale kinetic segregation of TCR and CD45 in engaged microvilli facilitates early T cell activation. *Nat. Commun.* 9:732. https://doi.org/10.1038/s41467-018-03127-w

Richie, L.I., P.J.R. Ebert, L.C. Wu, M.F. Krummel, J.J.T. Owen, and M.M. Davis. 2002. Imaging synapse formation during thymocyte selection: Inability of CD3ζ to form a stable central accumulation during negative selection. *Immunity*. 16:595–606. https://doi.org/10.1016/S1074-7613(02)00299-6

Rossboth, B., A.M. Arnold, H. Ta, R. Platzer, F. Kellner, J.B. Huppa, M. Brameshuber, F. Baumgart, and G.J. Schütz. 2018. TCRs are randomly distributed on the plasma membrane of resting antigen-experienced T cells. *Nat. Immunol.* 19:821–827. https://doi.org/10.1038/s41590-018-0162-7

Sage, P.T., L.M. Varghese, R. Martinelli, T.E. Sciuto, M. Kamei, A.M. Dvorak, T.A. Springer, A.H. Sharpe, and C.V. Carman. 2012. Antigen recognition is facilitated by invadosome-like protrusions formed by memory/effector T cells. *J. Immunol.* 188:3686–3699. https://doi.org/10.4049/jimmunol.1102594

Salter, A.I., A. Rajan, J.J. Kennedy, R.G. Ivey, S.A. Shelby, I. Leung, M.L. Templeton, V. Muhunthan, V. Voillet, D. Sommermeyer, et al. 2021. Comparative analysis of TCR and CAR signaling informs CAR designs with superior antigen sensitivity and in vivo function. *Sci. Signal.* 14: eabe2606. https://doi.org/10.1126/scisignal.abe2606

Schamel, W.W.A., I. Arechaga, R.M. Risueño, H.M. van Santen, P. Cabezas, C. Risco, J.M. Valpuesta, and B. Alarcón. 2005. Coexistence of multivalent and monovalent TCRs explains high sensitivity and wide range of response. *J. Exp. Med.* 202:493–503. https://doi.org/10.1084/jem.20042155

Scharping, N.E., D.B. Rivadeneira, A.V. Menk, P.D.A. Vignali, B.R. Ford, N.L. Rittenhouse, R. Peralta, Y. Wang, Y. Wang, K. DePeaux, et al. 2021. Mitochondrial stress induced by continuous stimulation under hypoxia rapidly drives T cell exhaustion. *Nat. Immunol.* 22:205–215. https://doi.org/10.1038/s41590-020-00834-9

Schmid, D.A., M.B. Irving, V. Posevitz, M. Hebeisen, A. Posevitz-Fejfar, J.-C.F. Sarria, R. Gomez-Eerland, M. Thome, T.N.M. Schumacher, P. Romero, et al. 2010. Evidence for a TCR Affinity Threshold Delimiting Maximal CD8 T Cell Function. *J. Immunol.* 184:4936–4946. https://doi.org/10.4049/jimmunol.1000173

Sendra, G.H., C.H. Hoerth, C. Wunder, and H. Lorenz. 2015. 2D map projections for visualization and quantitative analysis of 3D fluorescence micrographs. *Sci. Rep.* 5:12457. https://doi.org/10.1038/srep12457

Shakiba, M., P. Zumbo, G. Espinosa-Carrasco, L. Menocal, F. Dündar, S.E. Carson, E.M. Bruno, F.J. Sanchez-Rivera, S.W. Lowe, S. Camara, et al. 2022. TCR signal strength defines distinct mechanisms of T cell dysfunction and cancer evasion. *J. Exp. Med.* 219:e20201966. https://doi.org/10.1084/jem.20201966

Stone, J.D., A.S. Chervin, and D.M. Kranz. 2009. T-Cell receptor binding affinities and kinetics: Impact on T-cell activity and specificity. *Immunology*. 126:165–176. https://doi.org/10.1111/j.1365-2567.2008.03015.x

Varma, R., G. Campi, T. Yokosuka, T. Saito, and M.L. Dustin. 2006. T cell receptor-proximal signals are sustained in peripheral microclusters and terminated in the central supramolecular activation cluster. *Immunity*. 25:117–127. https://doi.org/10.1016/j.immuni.2006.04.010

Vasioukhin, V., C. Bauer, M. Yin, and E. Fuchs. 2000. Directed actin polymerization is the driving force for epithelial cell-cell adhesion. *Cell.* 100:209–219. https://doi.org/10.1016/S0092-8674(00)81559-7

Yokosuka, T., K. Sakata-Sogawa, W. Kobayashi, M. Hiroshima, A. Hashimoto-Tane, M. Tokunaga, M.L. Dustin, and T. Saito. 2005. Newly generated T cell receptor microclusters initiate and sustain T cell activation by recruitment of Zap70 and SLP-76. *Nat. Immunol.* 6:1253–1262. https://doi.org/10.1038/ni1272

JCB

Supplemental material

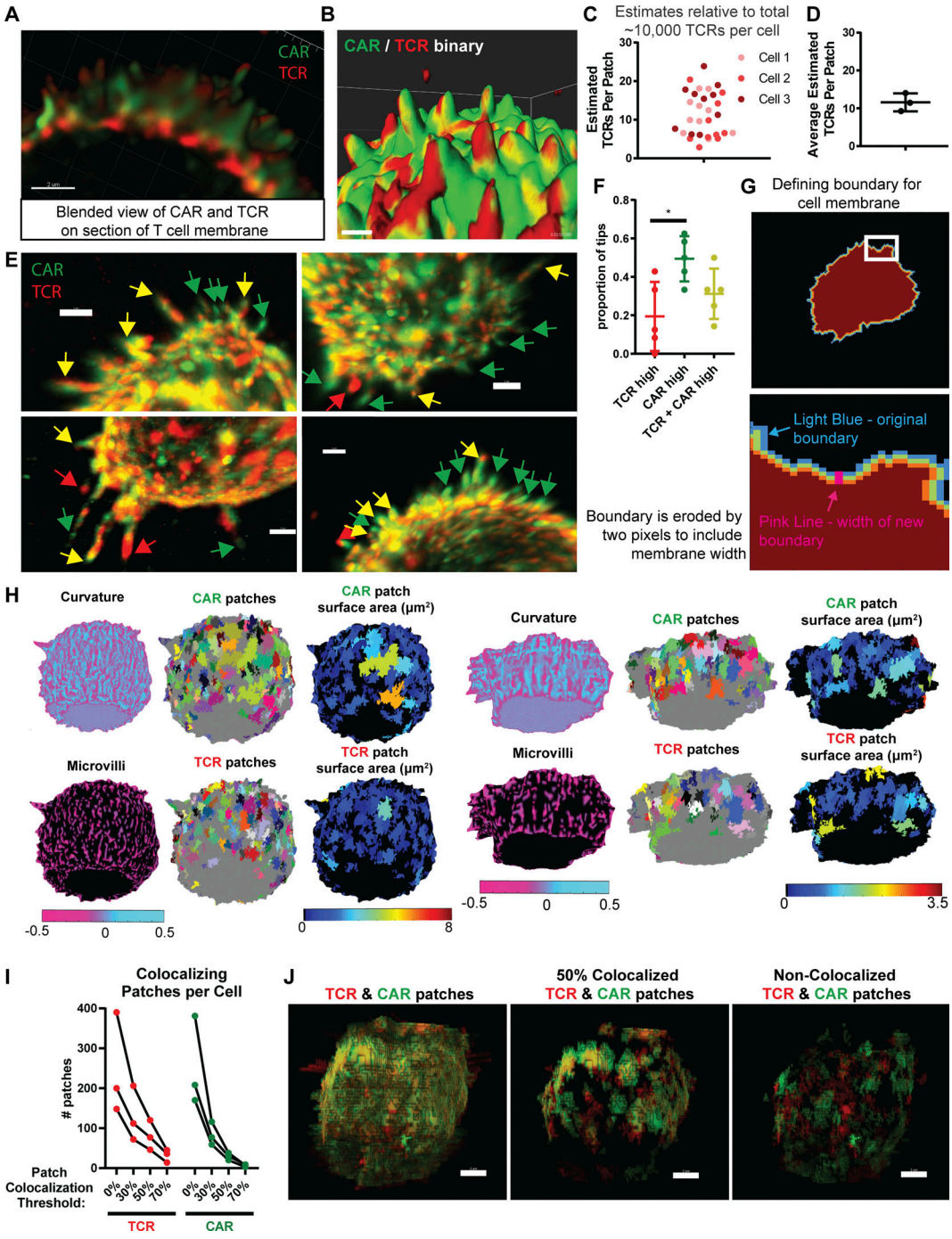

Figure S1. **Imaging TCR and CAR on the surface of isolated T cells. (A and B)** Blended view (A) and shaded binary (B) Imaris rendering of fixed anti-HER2 CAR T cell surface, as described in Fig. 1 A. Blended rendering shows section of 40 *z* slices. Scale bars are 2 µm. **(C and D)** Background intensity was subtracted from the sum of TCR intensity for a cell and divided by the approximate number of TCRs per cytotoxic T lymphocyte, which is at least ~10,000 according to Blichfeldt et al. (1996) and Labrecque et al. (2001), in order to estimate the fluorescence intensity per TCR for each cell. That is, the estimated intensity per TCR was derived for each cell by dividing the sum of the background-subtracted surface intensity by 10,000. Patch regions were cropped and the intensity sum (minus background) for each patch was divided by the estimated intensity per TCR. 10 patches per cell were analyzed (C) and averaged for each cell (D). **(E)** Regions of interest (in addition to Fig. 1 B) that were used for the manual count of MV tip receptor occupancy in Fig. 1, C and D. MV tips are marked as being high for TCR (red arrow), CAR (green arrow), or both (yellow arrow). Scale bars = 2 µm. **(F)** Proportion of MV tips per region of interest that were marked as high for TCR, CAR, or both. 41 tips across 5 regions and 3 cells were scored. **(G)** Schematic of method used to define the cell membrane boundary used in radial intensity profiles. Outer boundary defined for each *z*-slice based off change in channel intensity. **(H)** Two additional examples of cells analyzed as described in Fig. 2, A–F. **(I)** Clusters are quantified for increasing thresholds of co-localization. Left: Number of TCR clusters with 0, 30, 50, or 70% overlap with CAR clusters. Right: Number of CAR clusters with 0, 30, 50, or 70% overlap with TCR clusters. 3 cells were scored, and data points for each cell are connected by lines. **(J)** Maximum intensity projection of TCR and CAR patches rendered in Imaris. For each patch, the intensity is defined by the integrated intensity for that patch. All patches are shown on the left. Patches which are ≥50% co-localized (i.e., 50% of the CAR patch overlaps with TCR, and vice versa) and <50% co-localized are shown in middle and left panels, respectively.

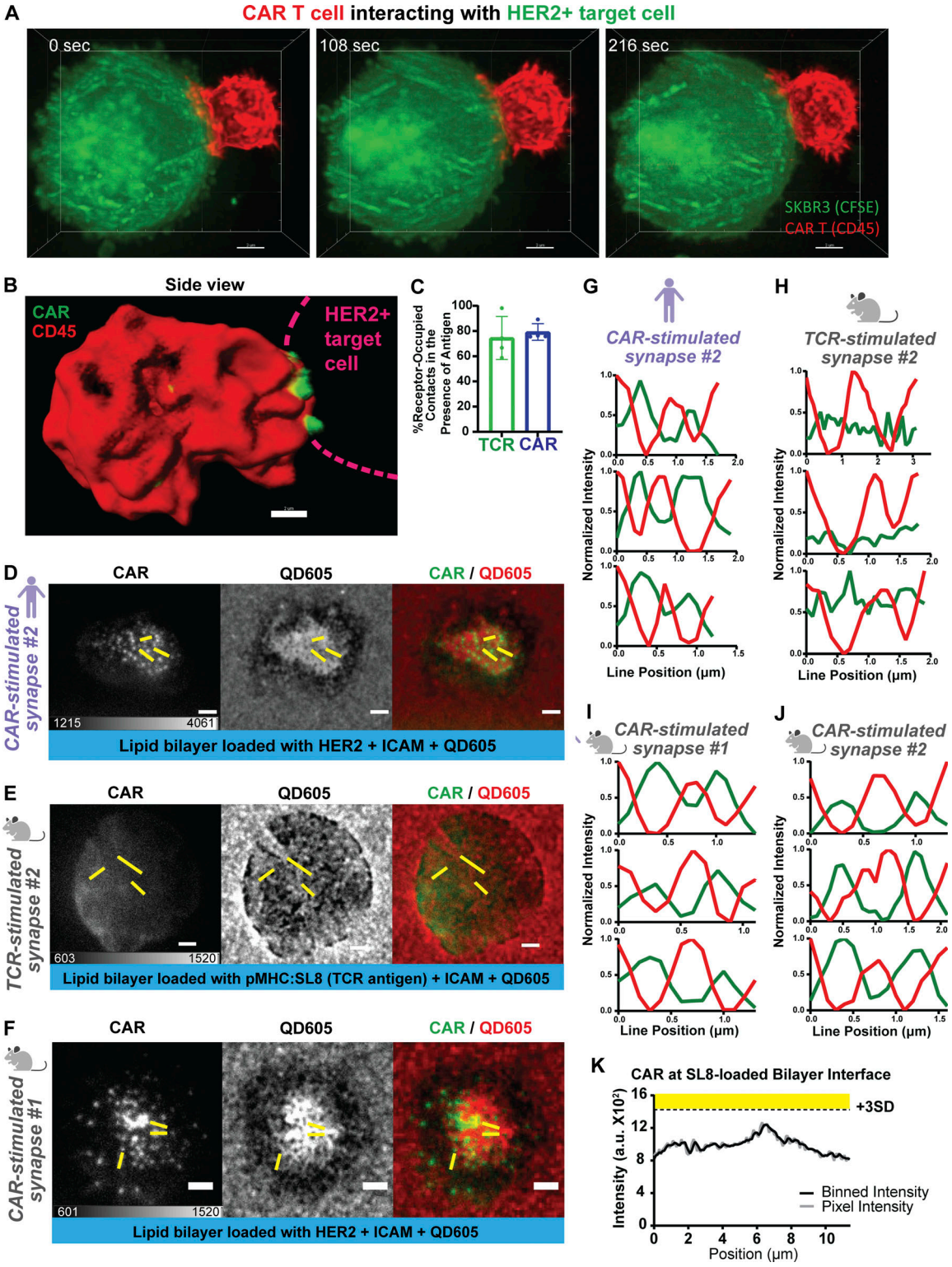

Figure S2. **Imaging CAR T cell:target interactions. (A)** Time-lapse of anti-CD45-Alexa647-stained CAR T cell interacting with CFSE-labelled HER2+ SKBR3 tumor cell by LLS imaging shows stable cell:cell interaction. Maximum intensity projection from Imaris is shown. Scale bar = 3 μm. **(B)** Additional example of a side-view of CAR T cell synapse with HER2+ SKBR3 target. CAR T cell was labeled and imaged as in Fig. 3, A–C but with CAR intensity based off endogenous mEmerald tag alone, without additional anti-MYC labeling. CAR localization without anti-MYC labeling shows the same enrichment of CAR in synaptic projections. Displayed in nomal shading mode in Imaris. Scale bar = 2 μm. **(C)** The percentage of MV close contacts occupied by receptor was not significantly different between the OT-I TCR and the LA CAR murine T cell synapses with cognate antigen (SL8:pMHC and 625 ng/well HER2). *n* = 4 cells, 55–133 close contacts were averaged for each cell. **(D–J)** Additional examples of cells prepared and analyzed by line scan as in Fig. 3, F–I. **(K)** 2D patch analysis of CAR in the TCR-stimulated synapse using a bin size of 300 nm—chosen in order to compare to clustering analysis in Fig. 1, F and G. No CAR intensity exceeded 3 SD above mean.

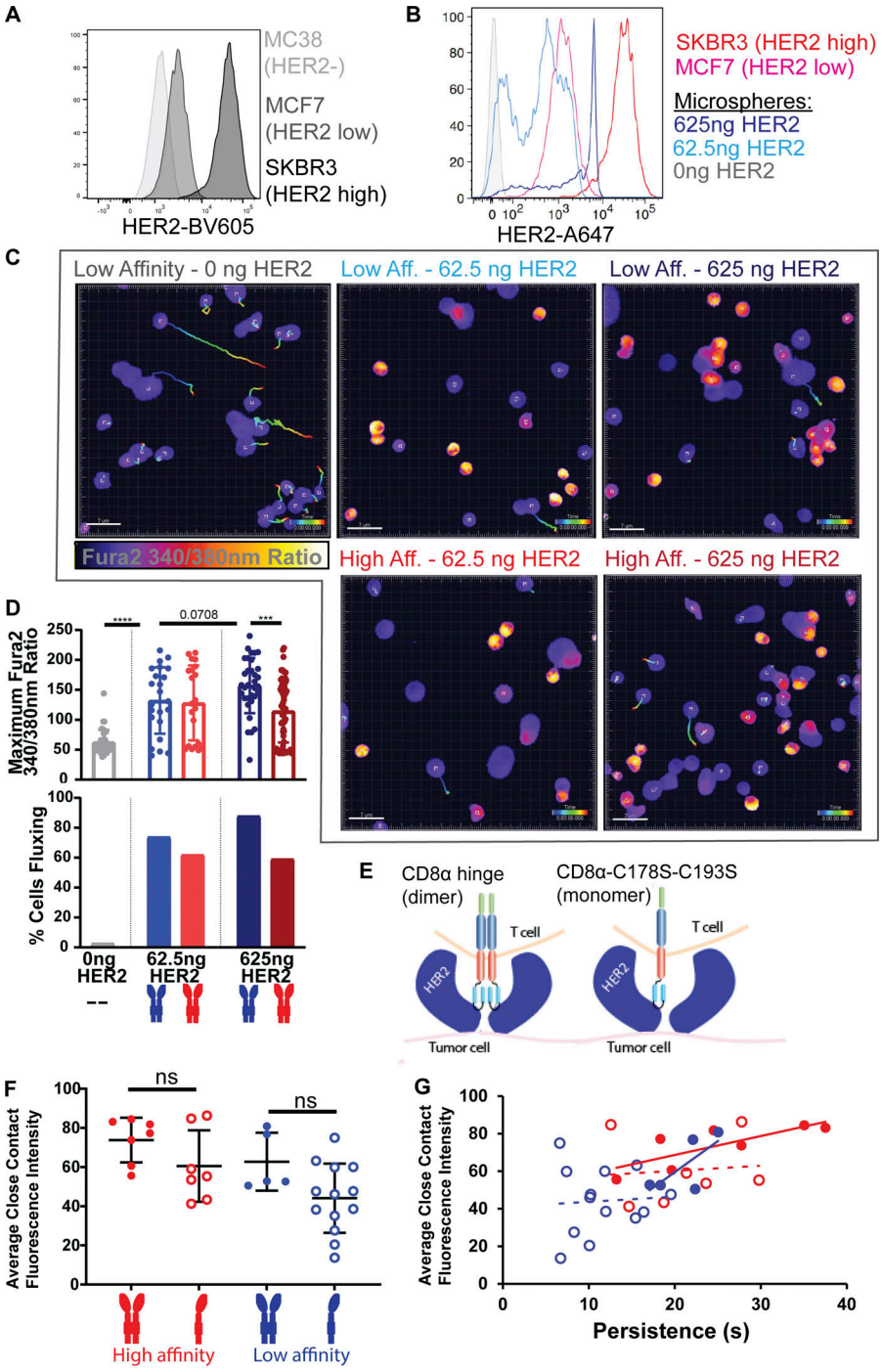

Figure S3. **CAR T cell calcium flux and close contact fluorescence. (A)** Anti-HER2-BV605 staining was performed on the human breast cancer cell lines MCF7 and SKBR3, plus murine MC38 cells as a HER2-negative control. Histogram overlay shows low and high HER2 expression for MCF7 and SKBR3, respectively. **(B)** Lipid bilayers with varying HER2 densities were built on 5 µm microspheres as standards for comparison to high-HER2 expressing SKBR3 and low-HER2 expressing MCF7s. Representative histogram from two independent experiments. **(C)** Fura-2 ratio images showing calcium flux (yellow) with tracks for interactions of CAR T cells with HER2-bilayers across antigen density and CAR affinity. Control well with no HER2 is shown on left. Images shown are at 3 min following addition of T cells. Scale bars are 7 µm. **(D)** Fura-2 ratio imaging shows calcium flux across affinity and HER2 density, with LA CAR T cells outperforming HA CAR T cells on high-HER2 loaded bilayers. Top: Maximum Fura-2 ratio for cells was quantified at 5.5 min following addition of T cells. Error bars represent SD (n = 37, 23, 21, 33, 66 cells per condition from left to right, respectively). Analyses are unpaired t tests. Bottom: Percentage of cells fluxing (defined as maximum Fura-2 ratio >100) for each condition was quantified at 5.5 min following addition of T cells. **(E)** Schematic of original anti-HER2 CAR, including two cysteines in the CD8 hinge region that form disulfide bond, and monomeric CAR made by mutation of those cysteines to serine (Hennecke and Cosson, 1993). **(F)** The average close contact CAR-mEmerald fluorescence intensity was not significantly different between monomers and dimers. Data is shown for at least 5 cells per condition across three experiments (n = 7, 7, 5, 13 cells per group from left to right, respectively, and ≥505 close contacts were averaged per cell). Error bars represent SD, analyses shown are unpaired t tests. **(G)** Average close contact CAR-mEmerald fluorescence intensity was plotted against persistence time following color schema in Q. Linear trend lines were added for each CAR type (monomers dashed).

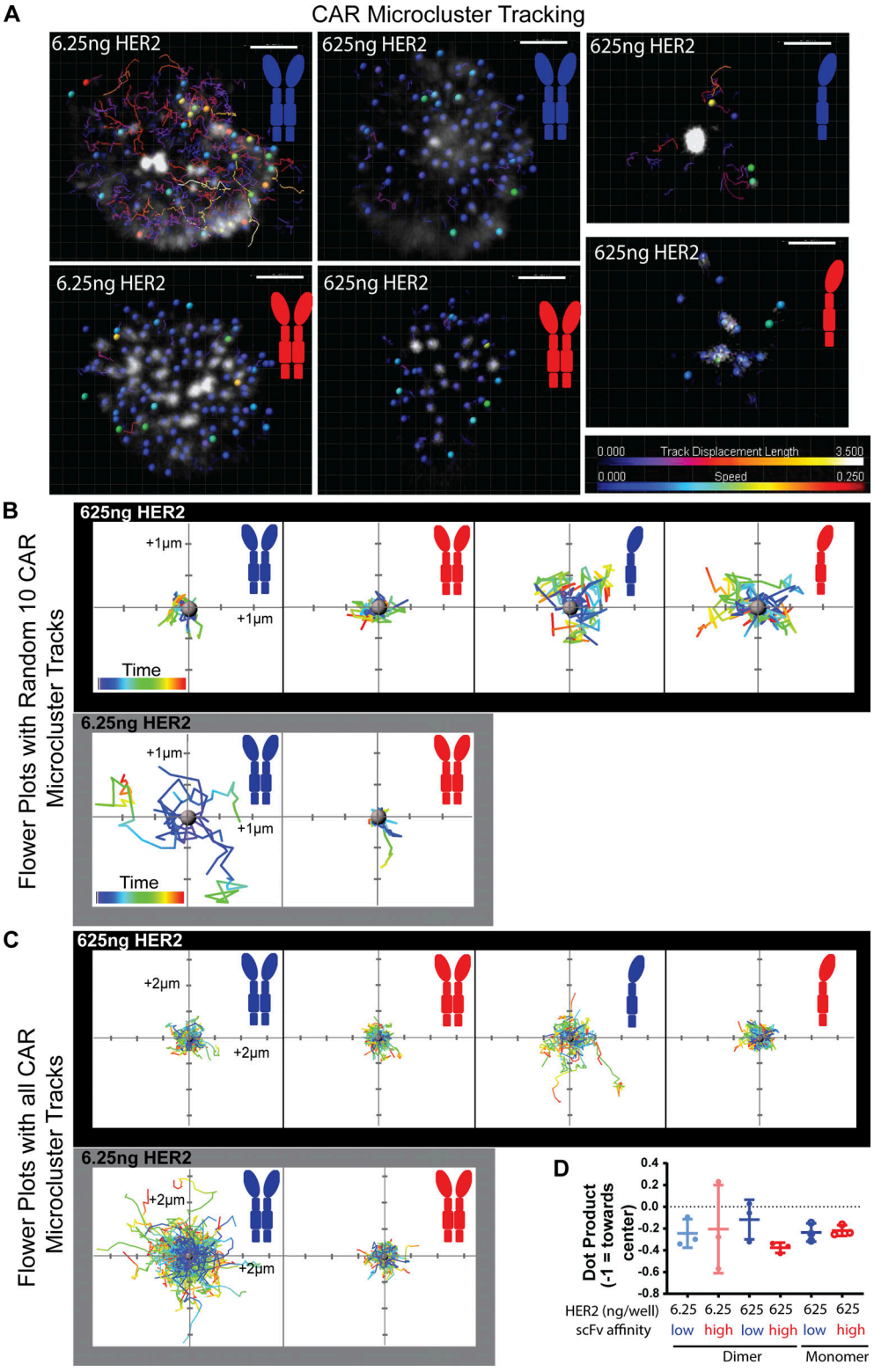

Figure S4. **CAR microcluster dynamics. (A)** TIRF imaging of CAR-mEmerald is shown with spots and tracks made in Imaris. Tracks analysis shows that HA CAR microclusters on low HER2 (6.25 ng/well) are not mobile, and on high HER2 (625 ng/well) only LA monomer is mobile. Scale bars = 3 μm. **(B)** A random 10 tracks are shown in flower plots for each condition. Top: Limited mobility is apparent for dimeric CARs on high-HER2 loaded bilayers. Bottom: On low-HER2 bilayers, LA CAR microclusters show increased mobility. Plots of low affinity dimer from Fig. 5 C are shown again here for comparison. **(C)** Flower plots are shown including all tracks for each cell. **(D)** The normalized dot product of V(rad) and V(i) was calculated for all tracks, where V(rad) = vector from synapse center to track start position and V(i) = vector from track start to track final position. Using this calculation, movements directly towards the center equal −1 and movements directly away from center equal 1. The average dot product for 3 cells were calculated (30–294 tracks per cell). No significant differences are identified in the direction of CAR microcluster movement across conditions. All n.s. by Tukey's multiple comparisons test.

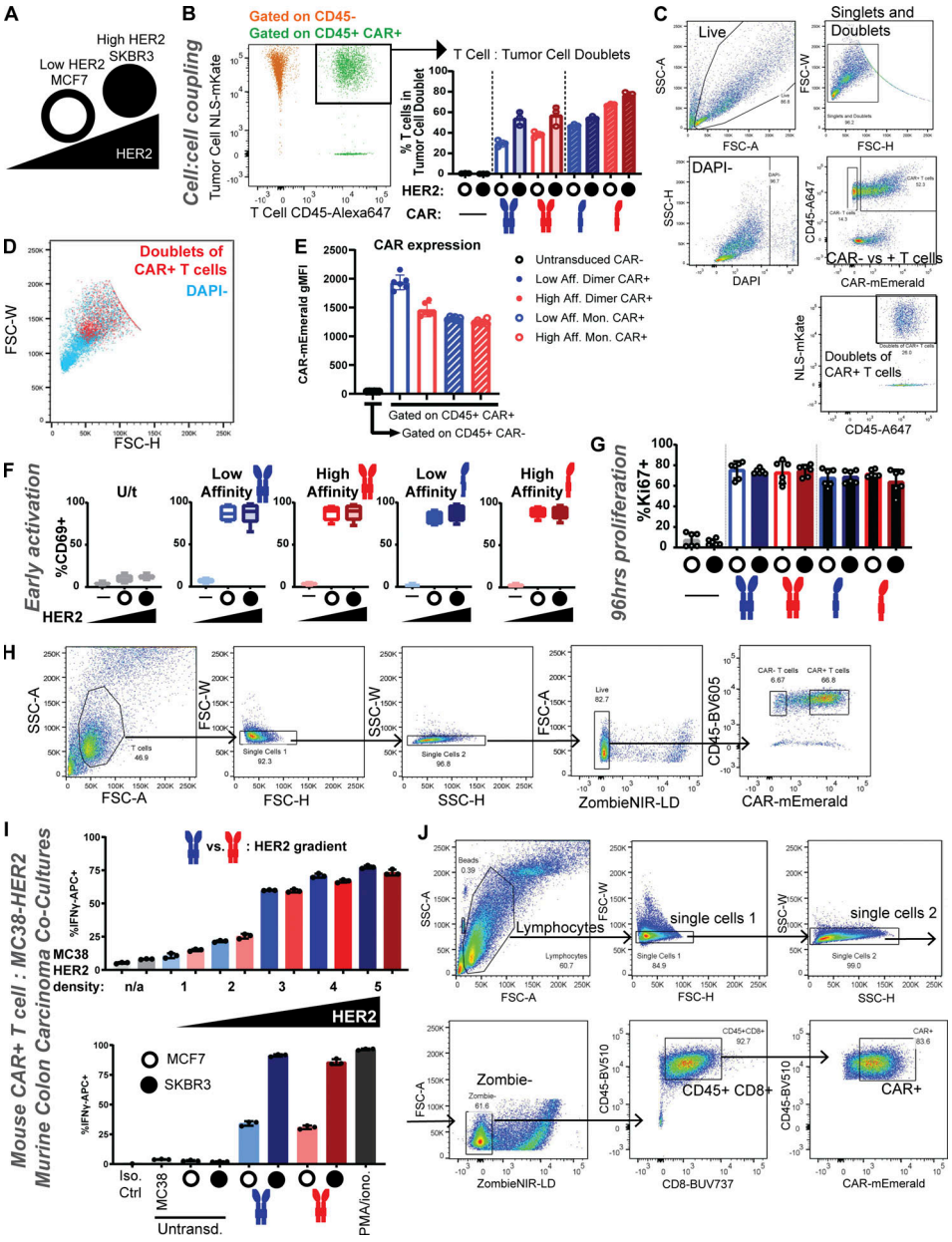

Figure S5. **Effects of CAR affinity, antigen density, and monomerization on CAR T cell activity. (A)** Low HER2-expressing MCF7 (open circle) and high HER2-expressing SKBR3 (solid circle) cell lines were used to assess differences between HER2 levels in cell-cell interactions in vitro. **(B)** MCF7 and SKBR3 cells expressing nuclear localization signal (NLS)-tagged mKate were incubated with anti-CD45-Alexa647-labeled T cells for 30 min. Coupling analysis was performed by gating inclusively for singlets and doublets. Cells were then gated on DAPI$^-$, CD45$^+$, and CAR+ (or CAR– for untransduced controls). Percentage of these cells that are mKate+ was reported as T cells in doublets with tumor cells (right). Representative dot plot for the HA monomeric CAR T cell/SKBR3 co-culture is shown overlaying the CD45$^-$ and CD45+CAR+ populations (left). Representative of three independent experiments is shown. **(C)** Gating strategy for coupling assay in B. Example data here is from a co-culture of LA dimeric CAR T cells with MCF7 target cells. **(D)** The entire DAPI- population in E is overlaid with the doublets of CAR+ T cells population. Plotting by FSC-H vs. FSC-W shows that the doublets of CAR+ T cells population falls in the expected region (above the singlets). **(E)** CAR gMFIs are shown for each receptor type. While there is some variability in expression, differences are within ∼2/3rds of the highest gMFI. Data shown are from a representative experiment (n = 6). **(F)** Early activation is similar across all CAR+ conditions with low and high HER2 at 18 h following co-incubation, as seen by anti-CD69-BUV395 positivity. Box and whiskers plot error bars showing minimum and maximum values (n = 12 samples per group pooled from four independent experiments and two donors). **(G)** Percentage of anti-Ki67-PE-eFluor 610 positive cells at 96 h following co-incubation, indicating entry into cell cycle, is similar across all CAR+ conditions with low and high HER2. Replicates from two independent experiments of different donors are pooled (n = 6). Error bars represent SD. **(H)** Gating strategy used for defining human CAR+ (and CAR–) T cells in flow cytometry experiments is shown. Example data shown here is from a co-culture of LA dimeric CAR T cells with SKBR3 target cells. **(I)** LA (blue) and HA (red) CARs were retrovirally expressed in primary mouse CD8$^+$ T cells. HER2-expressing MC38 cells were sorted into 5 bins of expression levels. MC38-HER2 (1-5) and parental MC38 (n/a) were cultured with CAR T cells for 18 h and then stained for IFN-γ. LA and HA CARs performed similarly. Isotype control, untransduced T cell, MCF7 (open circle), SKBR3 (filled circle), and PMA/ionomycin controls are shown below. n = 3 replicates per group. Data shown is representative of three independent experiments. **(J)** Gating strategy used for defining mouse CAR+ T cells in flow cytometry experiments following in vitro co-culture is shown. Example data shown here is from a co-culture of LA dimeric CAR T cells with MC38-HER2-high targets in normoxia.

Video 1. **LLS imaging of anti-HER2 CAR T cell.** Maximum intensity projection of anti-HER2 CAR-expressing T cell shown in Fig. 1 B. Location of coverslip, where signal intensity is low, is annotated in yellow. Anti-CD45-Alexa594, anti-MYC (CAR)-Alexa488, and TCR (OKT3)-APC signal is shown in cyan, green, and red, respectively.

Video 2. **LLS live cell imaging of anti-HER2 CAR T cell in synapse with HER2+ SKBR3 cell.** The normal shading view of the Imaris volume is shown for anti-HER2 CAR-expressing T cell shown in Fig. 3 A. The SKBR3 target cell is located above, as annotated in Fig. 3 A. Anti-CD45-Alexa647 and anti-MYC (CAR)-Alexa488 signals are shown in red and green, respectively. Scale bar = 2 µm. Time resolution per frame is 4.7 s, and total video is 20 frames (89.3 s).

Video 3. **Individual close contacts imaged by SCM TIRF microscopy.** QD605 signal is shown for one field of view for LA (top) and high-affinity HA (bottom) CAR T cells interacting with HER2-loaded bilayer (6.25 ng/well). Holes in QD605 signal show location of microvillar close contacts. HA close contact stably persists in same field of view, while LA CAR T cell contacts appear and disappear from field of view throughout imaging. Scale bar is 0.2 µm. Time resolution per frame is 2.4 s, and total video is 40 frames (93.6 s).

Video 4. **Fura-2 calcium flux imaging of LA and HA CAR T cells on low- and high-HER2 bilayers.** Fura-2 340/380 nm ratio channel with tracking is shown for (A) LA/0 ng HER2, (B) LA/62.5 ng HER2, (C) LA/625 ng HER2, (D) HA/62.5 ng HER2, and (E) HA/625 ng HER2 (from top to bottom) CAR T cells interacting with loaded bilayers. Calcium flux (yellow) is seen for interactions of CAR T cells with HER2-bilayers across antigen density and CAR affinity, relative to no HER2 control (A). Scale bar is 7 µm. Imaging was initiated at 3 min following addition of T cells to wells. Time resolution per frame is 1.5 s, and total video is 100 frames (148.5 s).

Video 5. **CAR microcluster tracking analysis—LA dimer on low HER2 bilayer.** TIRF imaging of CAR-mEmerald is shown for LA dimeric CAR on bilayer loaded with 6.25 ng/well. Spots show position of microclusters used for tracking. Scale bar is 3 µm. Time resolution per frame is 2.4 s, and total video is 40 frames (93.6 s).

Video 6. **CAR microcluster tracking analysis—HA dimer on low HER2 bilayer.** TIRF imaging of CAR-mEmerald is shown for HA dimeric CAR on bilayer loaded with 6.25 ng/well. Spots show position of microclusters used for tracking. Scale bar is 3 µm. Time resolution per frame is 2.4 s, and total video is 40 frames (93.6 s).

Video 7. **CAR microcluster tracking analysis—LA dimer on high HER2 bilayer.** TIRF imaging of CAR-mEmerald is shown for LA dimeric CAR on bilayer loaded with 625 ng/well. Spots show position of microclusters used for tracking. Scale bar is 3 µm. Time resolution per frame is 2.4 s, and total video is 40 frames (93.6 s).

Video 8. **CAR microcluster tracking analysis—HA dimer on high HER2 bilayer.** TIRF imaging of CAR-mEmerald is shown for HA dimeric CAR on bilayer loaded with 625 ng/well. Spots show position of microclusters used for tracking. Scale bar is 3 µm. Time resolution per frame is 2.4 s, and total video is 40 frames (93.6 s).

Video 9. **CAR microcluster tracking analysis—LA monomer on high HER2 bilayer.** TIRF imaging of CAR-mEmerald is shown for LA monomeric CAR on bilayer loaded with 625 ng/well. Spots show position of microclusters used for tracking. Scale bar is 3 µm. Time resolution per frame is 2.4 s, and total video is 40 frames (93.6 s).

Video 10. **CAR microcluster tracking analysis—HA monomer on high HER2 bilayer.** TIRF imaging of CAR-mEmerald is shown for HA monomeric CAR on bilayer loaded with 625 ng/well. Spots show position of microclusters used for tracking. Scale bar is 3 µm. Time resolution per frame is 2.4 s, and total video is 40 frames (93.6 s).

Provided online are Table S1 and Table S2. Table S1 lists mutations in CAR scFv (mutCD45) and CD8α hinge/TMD (monomer). Table S2 lists antibodies referenced for flow cytometry and imaging experiments.